Correcting laser scanning intensity recorded in a cave environment for high-resolution lithological mapping: A case study of the Gouffre Georges, France

Michaela Nováková, Michal Gallay, Jozef Šupinský, Eric Ferré, Riccardo Asti, Michel de Saint Blanquat, Flora Bajolet, Patrick Sorriaux

Correcting laser scanning intensity recorded in a cave environment for high-resolution lithological mapping: a case study of the Gouffre Georges, France

Michaela Nováková[1,*], Michal Gallay[1], Jozef Šupinský[1], Eric Ferré[2], Riccardo Asti[3,4], Michel de Saint Blanquat[5], Flora Bajolet[5], Patrick Sorriaux[6]

Affiliations:

[1]Institute of Geography, Faculty of Science, Pavol Jozef Šafárik University in Košice, Jesenná 5, 04001 Košice, Slovakia

[2]School of Geosciences, University of Louisiana at Lafayette, Lafayette, LA 70504, USA

[3]Université Côte d'Azur, CNRS, Observatoire de la Côte d'Azur, IRD, Géoazur, France

[4]Univ Rennes, CNRS, Géosciences Rennes, UMR 6118, 35000 Rennes, France

[5]Géosciences Environnement Toulouse, Université de Toulouse, CNRS, IRD, UPS, CNES, 31400 Toulouse, France

[6]Spéléo Club du Haut Sabarthez, 09400 Tarascon sur Ariège, France

*Corresponding author, e-mail address: michaela.novakova@student.upjs.sk

Abstract

Active remote sensing by laser scanning (LiDAR) has markedly improved the mapping of a cave environment with an unprecedented level of accuracy and spatial detail. However, the use of laser intensity simultaneously recorded during the scanning of caves remains unexplored despite it having promising potential for lithological mapping as it has been demonstrated by many applications in open-sky conditions. The appropriate use of laser intensity requires calibration and corrections for influencing factors, which are different in caves as opposed to the above-ground environments. Our study presents an efficient and complex workflow to correct the recorded intensity, which takes into consideration the acquisition geometry, micromorphology of the cave surface, and the specific atmospheric influence previously neglected in terrestrial laser scanning. The applicability of the approach is demonstrated on terrestrial LiDAR data acquired in the Gouffre Georges, a cave located in the northern Pyrenees in France. The cave is unique for its geology and lithology allowing for observation, with a spectacular continuity without any vegetal cover, of the contact between marble and lherzolite rocks and tectonic structures that characterize such contact. The overall accuracy of rock surface classification based on the corrected laser intensity was over 84 %. The presence of water or a wet surface introduced bias of the intensity values towards lower values complicating the material discrimination. Such conditions have to be considered in applications of the recorded laser intensity in mapping underground spaces. The presented method allows for putting geological observations in an absolute spatial reference frame, which is often very difficult in a cave environment. Thus, laser scanning of the cave geometry assigned with the corrected laser intensity is an invaluable tool to unravel the complexity of such a lithological environment.

Key words

Intensity correction, Terrestrial laser scanning, LiDAR, Cave, Lithological mapping

1. Introduction

Laser scanning has demonstrated its extensive potential for landscape mapping over the last few decades (Eitel et al., 2017). The majority of applications focus on acquiring 3D coordinates to parametrise the three-dimensional (3D) structure of the landscape while a smaller portion of published research makes use of the recorded intensity of the backscattered laser pulse, related to the surface parameters and recorded for each point position. As a result of laser scanning, a 3D point cloud is generated, capturing morphology in a high level of spatial detail along with specific spectral properties of the surface surrounding the laser scanner. The advantage of this active remote sensing technique has been employed in cave mapping, where the complex morphology and limited light conditions challenge studying the cave surface by direct contact or optical methods at a high spatial resolution (Gallay et al., 2015). Compared to the methods traditionally used in speleology and cave surveying, such as traversing with the compass or total station, laser scanning reduces the work time and is light-independent, unlike digital photogrammetry (Idrees and Pradhan, 2016a).

In the last decade, terrestrial laser scanning (TLS) of caves has been deployed in a range of scientific applications, e.g., archaeology (Burens et al., 2014; Kruger et al., 2016; Landeschi et al., 2019), geology and geomorphology (Silvestre et al., 2015; Fabbri et al., 2017; De Waele et al., 2018), geomorphometry (Gallay et al., 2016), and biospeleology (Azmy et al., 2012; McFarlane et al., 2015). The acquired 3D geometry is also beneficial for mapping and evaluating the ice surface morphology change (Milius and Petters, 2012; Berenguer-Sempere et al., 2014; Šupinský et al., 2019), assessing the natural hazards and collapse susceptibility (Santo et al., 2017; Idrees and Pradhan, 2018), for general visualization and creation of a 3D cave model (Núñez et al., 2013; Cosso et al., 2014), and creating a highly-detailed cave map (Šupinský et al., 2022). Recent studies also demonstrated the potential of using the TLS intensity for cave environment research, e.g., for the discernment of micro-morphologies, different speleogenetic phases, karstification processes, and identification of cave arts and engravings (Idrees and Pradhan, 2017; Jalandoni et al., 2021). As well in biospeleology, the

intensity data can be used for non-intrusive population surveys and species recognition for cave fauna, especially roosting bats (Azmy et al., 2012) or birds (Idrees and Pradhan, 2016b), with satisfactory results for the selected cave sections even without any radiometric processing or intensity calibration. However, the influence of individual factors is noticeable particularly for varying scanning ranges and data-overlaps of multiple scanning positions acquired in an extensive cave complex.

The recorded intensity values are influenced by several factors, including surface properties, sensor parameters, acquisition geometry, and atmospheric conditions during scanning (Kaasalainen et al., 2011; Tan and Cheng, 2016). However, the atmospheric effect on laser signal propagation is often neglected in TLS. The rationale is in the short scanning ranges within which the effect of the atmospheric attenuation is considered to be constant if the atmospheric conditions remain unchanged during scanning and the air transmittance is very high (Carrea et al., 2016). The content of the surface moisture also affects the recorded intensity values which decrease with increasing moisture for water absorbs the near-infrared wavelengths (Franceschi et al., 2009). Therefore, in an extensive cave environment with variable dimensions comprising narrow passages leading to grand domes and specific atmospheric conditions, the effect of the influencing factors is considerable. Moreover, the multi-scan TLS intensity data obtained by different acquisition campaigns are not directly comparable (Tan et al., 2015). For extraction intensity values proportional primarily to the scanned surface reflectance, other influencing factors should be eliminated. Kashani et al. (2015) provide a comprehensive overview of the processing methods of the intensity values mainly divided into theoretical correction models based on the radar equation (Höfle and Pfeifer, 2007; Wagner, 2010) and data-driven empirical models (Höfle and Pfeifer, 2007; Teo and Yu, 2015; Xu et al., 2017), both with specific limitations. Acquisition geometry is defined by the scanning range and the incidence angle, i.e., the angle between the incident laser beam and the normal vector of the surface (Soudarissanane et al., 2011). Kaasalainen et al. (2011) showed that the effect of incidence angle is caused by the target surface properties, whereas the distance effect is mainly influenced by the instrumental factors and does not entirely follow the radar equation range function. Specifically, near-

distance intensities up to several meters deviate from the radar range equation and vary across different laser scanning systems. Moreover, the correction of the incidence angle effect using Lambert´s cosine law is not sufficient, especially for the natural surfaces, which do not behave as Lambertian reflectors (Carrea et al., 2016; Tan et al., 2016).

Current remote sensing techniques, including passive photogrammetry and hyperspectral imaging, allow for high-resolution mapping of difficult-to-access geological outcrops (Lorenz et al., 2021; Thiele et al., 2021). Recent studies have also demonstrated the potential of the corrected TLS intensity data for geological mapping and distinguishing rock types within the aboveground rock outcrops (Penasa et al., 2014; Matasci et al., 2015; Carrea et al., 2016; Živec et al., 2019), without the need of eliminating the atmospheric attenuation effect. The presented paper aims to define the method of correcting the laser scanning intensity acquired in the cave environment, where the variable dimensions, specific atmospheric conditions, and limited light conditions restrict the employment of optical sensing or direct use of the recorded intensity for the material differentiation. The proposed intensity correction approach combines the data-driven methods for the distance effect correction, applying correction of the incidence angle effect using the Oren-Nayar model (Carrea et al., 2016) and eliminating the atmospheric attenuation effect with the data-driven coefficients.

The proposed method was demonstrated on the data acquired in a cave known as Gouffre Georges to distinguish two distinct rock types within the TLS point cloud. Part of the cave was formed along the lithological contact between marble and lherzolite, which name was derived from its type locality, the Étang de Lers (previously Étang de Lherz). This ultramafic igneous rock was formed in the upper mantle and is rarely observable exposed on the surface (Sorriaux et al., 2019). The corrected intensity values allow putting geological observations in an absolute spatial reference frame, which is often very difficult in a cave environment. Such results provide a combined view of underground and surficial geological settings which improves studying geological structures and understanding their formation. Along with conventional near-infrared spectroscopy the method can become applicable in mining for underground mapping and mineral exploration (Laukamp et al., 2012; Guha et al., 2015).

1.1. Background on laser scanning intensity

Laser scanning operates on the same physical principle as radar; therefore, the radar equation can be applied to describe the main factors affecting the received signal strength (Wagner, 2010), providing a theoretical basis for the model-driven approach of the intensity correction. This equation relates to the received power P_r, transmitted pulse power P_t and other parameters referring to the acquisition geometry and sensor, atmospheric, and target properties.

$$P_r = \frac{P_t D_r^2}{4\pi R^4 \beta_t^2} \eta_{sys} \eta_{atm} \sigma \quad \text{(Eq. 1)}$$

Range R represents distance between the sensor and object, D_r is a diameter of the sensor receiver aperture, β_t is the transmitter beamwidth, η_{sys} and η_{atm} are system and atmospheric transmission factors, respectively. All target parameters are combined into backscatter cross-section σ expressing the backscattering target characteristics as a function of the target size, reflectance, and scattering directionality (Wagner et al., 2006).

Assuming that the scanned area is an extended target larger than a laser footprint size and its surface has Lambertian scattering characteristics, the backscatter cross-section can be expressed as (Carrea et al., 2016; Xu et al., 2017):

$$\sigma = \pi \rho_\lambda R^2 \beta_t^2 \cos\alpha \quad \text{(Eq. 2)}$$

where ρ_λ is the target surface reflectance at a certain wavelength λ and α is the incidence angle, the angle between the surface normal vector and the incident laser beam.

Parameters P_t, D_r and η_{sys} depend on the sensor and can be considered constant for a specific device as well as the atmospheric attenuation η_{atm} for the TLS data acquisition under stable conditions (Xu et al., 2017). After substituting Equation (2) into Equation (1) and simplifying for constants, the radar equation can be written as:

$$P_r = \rho_\lambda R^{-2} \cos\alpha \quad \text{(Eq. 3)}$$

148 The intensity value I represents the measure of the signal strength obtained by converting and
149 amplifying the received power P_r, which is transformed into Digital Number (DN) as a scaled integer
150 value (Höfle and Pfeifer, 2007; Tan et al., 2016) or provided in arbitrary units depending on the LiDAR
151 device. As the intensity is generally proportional to the received power, then:

152 $$I \propto P_r \propto \rho_\lambda R^{-2} \cos\alpha \quad \text{(Eq. 4)}$$

153 ## 2. Study site

154 The LiDAR data were acquired by laser scanning in the Gouffre Georges, Ariège, France (Fig. 1).
155 The cave formed in between the Mesozoic carbonate cover of the northern Pyrenees, and peridotites
156 on the eastern slope of the Mont Béas, in the vicinity of the Étang de Lers. The cave is unique because
157 it is carved along the tectonic contact between two distinctive rock units: variably serpentinized
158 lherzolites of mantle origin and Jurassic and lower Cretaceous carbonate rocks. The degree of
159 serpentinization of the peridotites varies greatly at the scale of the Lherz Massif and tends to increase
160 near contacts, faults, and shear zones. The unserpentinized lherzolite consists primarily of olivine
161 (Fo89-Fo92), enstatite, Cr-diopside, and Cr-spinel (Le Roux et al., 2007). The main serpentines include
162 chrysotile and, to a minor extent, antigorite. The carbonate rocks are massive or banded marbles, and
163 monomictic to polymictic, locally dolomitic carbonate breccias. The most common minerals include
164 calcite, dolomite, scapolite, phlogopite, and quartz. The dark bands in the marbles tend to be blueish
165 due to the presence of scapolite and are continuous over several meters.

166 The terrestrial laser scanning was performed in one branch of the cave corridors accessible via the
167 closable entrance Tube at the altitude of 1390 m. Continuously descending narrow entrance passage
168 after about 70 meters enters a large dome of the Grande Galerie with over 10 to 15 m height, 20 m
169 width and length of 130 m. The contact between marble and lherzolite is very well preserved in this
170 dome. The dome continues down to the Salle de la Famine dome which formed in marble and marble
171 breccia, but lherzolite debris was transferred from the upper parts forming the scree on the cave
172 bottom. Overall, the surveyed part of the cave extended about 200 meters horizontally and 200 meters

vertically with a general slope of the cave corridors of 45°. Scanning in the Gouffre Georges challenged the standard outdoor terrestrial laser scanning by a steep ground surface often with unstable scree or passing through narrow corridors and vertical sections.

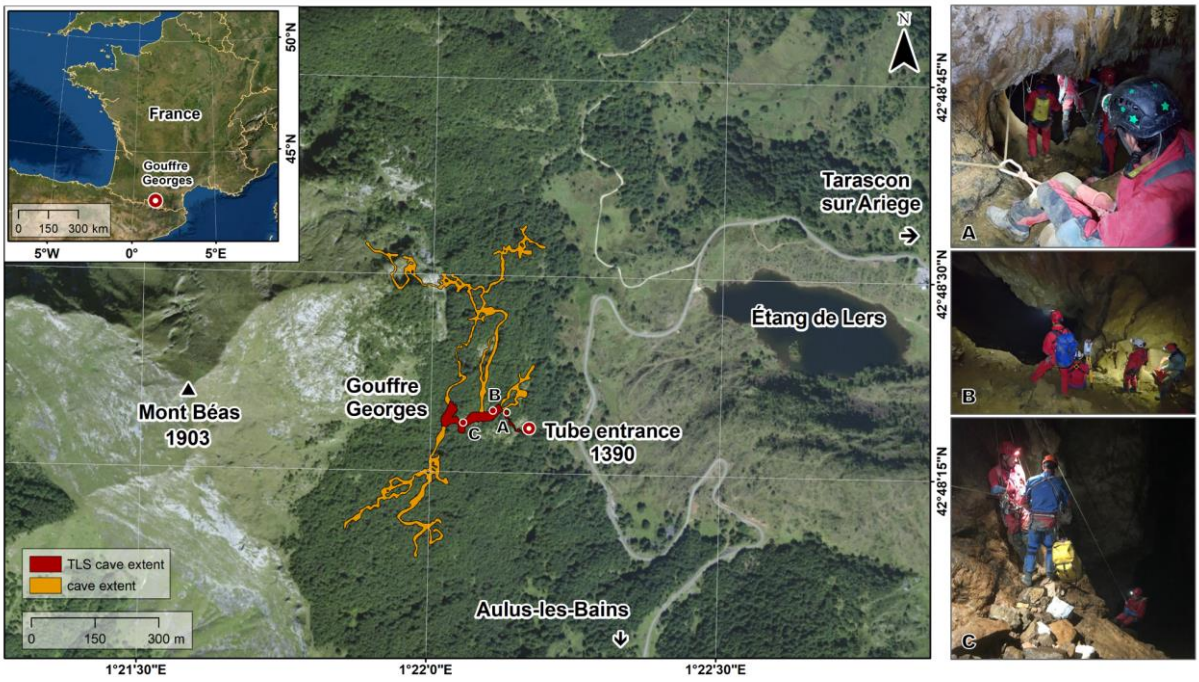

Fig. 1. Location of the Gouffre Georges. Selected parts for the TLS survey (red) of the Gouffre Georges cave complex (orange) are accessible via the entrance Tube at the altitude of 1390 m. The photographs A, B, C illustrate the cave space and surveying conditions in different parts located in the map. Base map: ©2021 Esri

The scanned part of the cave provides a special opportunity to directly observe the rare geological and lithological setting. More than 40 lherzolite bodies crop out in the Pyrenean belt (Monchoux, 1970). These rocks have been exhumed during the Albian-Cenomanian rifting phase (e.g., Lagabrielle et al., 2010) and have been then uplifted and put in their present-day position during the Late Cretaceous-Tertiary Pyrenean orogeny (Vergés et al., 2002; Saspiturry et al., 2020a). The North Pyrenean Zone, where such ultramafic rocks crop out, represents then the suture zone between the Iberian and the Eurasian plates. In the last decade, renewed interest has grown in the scientific community regarding the geologic history of the Pyrenean lherzolites (e.g., Lagabrielle and Bodinier, 2008; Jammes et al., 2009; Clerc and Lagabrielle, 2014). In particular, active debates have developed concerning the tectonic style related to the exhumation of mantle rocks during the Cretaceous rifting

(e.g., Masini et al., 2014; Asti et al., 2019; Lagabrielle et al., 2019a, b; Saspiturry et al., 2019), its thermal implications (Clerc et al., 2015; Lagabrielle et al., 2016; Ducoux et al., 2019; Duretz et al., 2019; Saspiturry et al., 2020b), the kinematics of this extensional phase (e.g., Jammes et al., 2009; Tavani et al., 2018; Angrand et al., 2020) and the genesis of lherzolite-bearing breccia which is often found in association with the ultramafic bodies all along the North Pyrenean Zone (Lagabrielle and Bodinier, 2008; Debroas et al., 2010; Clerc et al., 2012; Saint Blanquat et al., 2016). The Lherz ultramafic massif is a key locality to find important constraints to all these scientific questions (see Clerc et al., 2012 and Lagabrielle et al., 2016 for exhaustive reviews).

3. Data and methods

The work undertaken in the presented research involved the workflow shown in Fig. 2. The research commenced with the 3D mapping in the cave by TLS survey and processing of the recorded data. It was followed by scanning in laboratory conditions. Subsequently, the effects of the acquisition geometry and different surface conditions were analysed and the parameters required for the corrections steps were derived. After correcting the intensity of each scan for the effect of distance and incidence angle, the derivation of the atmospheric attenuation coefficient was performed based on the data in overlaps of the individual scans. The last step involved denoising, i.e., removing the outliers by the nearest neighbour analysis and interpretation of the obtained corrected intensity values. Each step of the workflow is characterized in the following subsections.

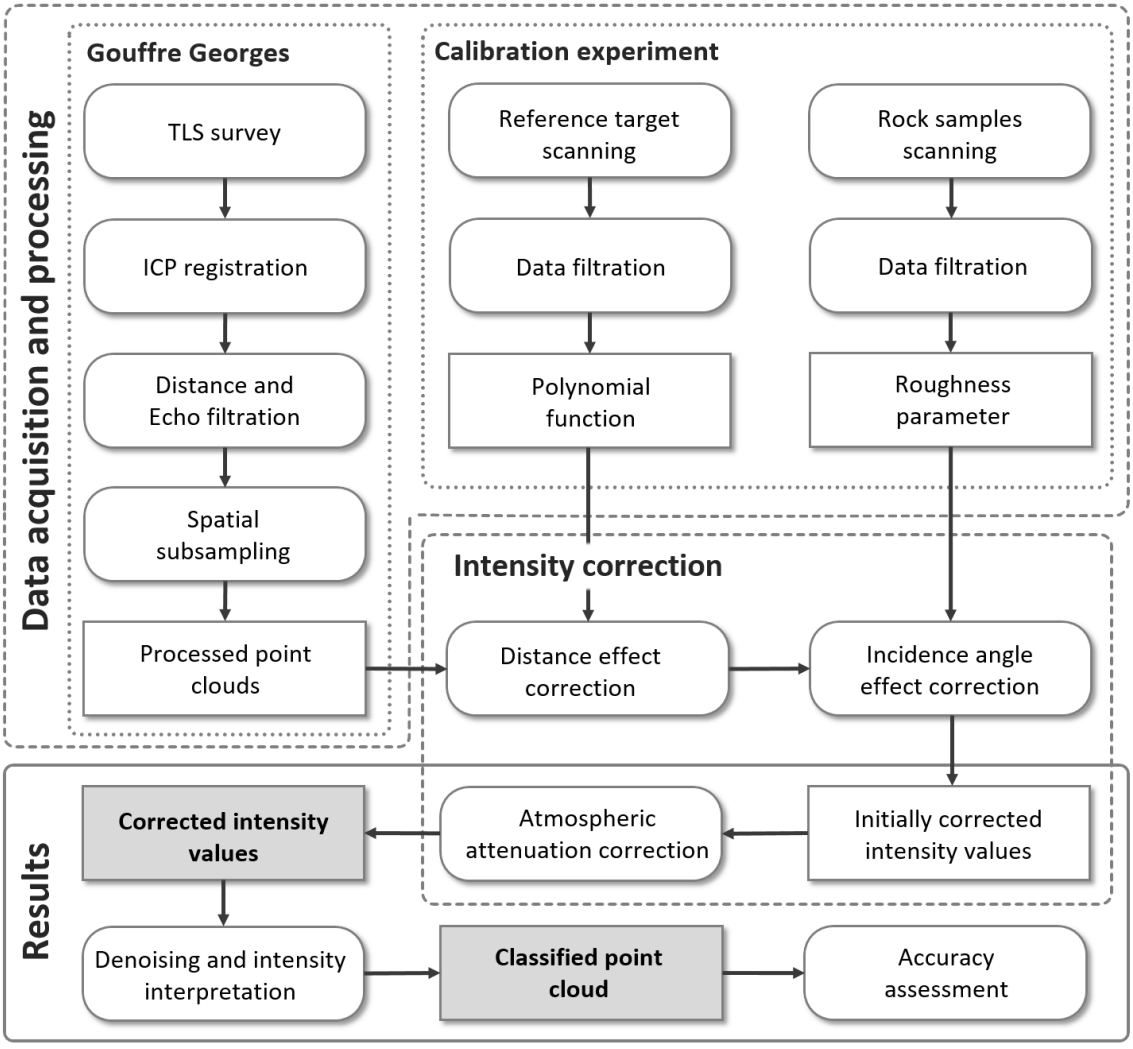

Fig. 2. Schematic workflow of processing the data obtained by TLS survey and experimental scanning and subsequent parameter estimation for the intensity correction.

3.1. Cave laser scanning and data processing

The selected part of the cave was scanned from 47 positions in total (Fig. 3) representing the entrance narrow passage from Tube and the domes of Salle de la Famine and Grande Galerie. Data were acquired by the time-of-flight TLS RIEGL VZ-1000 with 360° horizontal and 100° vertical field of view emitting near-infrared laser pulses laser of 1,550 nm wavelength (RIEGL, 2015). The specification for the used TLS device is listed in Tab. 1. The robust construction of the device enables scanning in adverse conditions and prevents its damage during transportation and abseiling in the cave. Besides

high-ranging precision and accuracy, implemented echo digitization and on-line waveform processing enables assigning additional attributes to each point measurement (Pfenningbauer and Ullrich, 2010).

Tab. 1. Specification for the used laser scanner

RIEGL VZ-1000			
Laser wavelength	1550 nm	Accuracy	8 mm
Field of view	100° x 360°	Precision	5 mm
Pulse repetition rate	70 – 300 kHz	Beam divergence	0.3 mrad
Maximum range	1400 m	Initial beam diameter	7 mm
Minimum range	2.5 m	Beam-widening	30 mm per 100 m

The first 26 positions were captured with an angular step width set to Panorama 40 with an angular increment of 0.04° between two successive emitted laser beams. This ensured a high density of points and detailed scanning in those cave sections where terrain and wall geometry are complex and rock boundaries are well detectable. The remaining 21 positions were located in the narrow passage from the Grande Galerie to the cave entrance of Tube. This was performed to geolocate the cave interior with the above-ground terrain surface and global geodetic coordinate system (i.e., global data registration) using the scanner's inbuilt GNSS receiver. In these narrow parts, the scanning density of Panorama 60 with an angular increment of 0.06° was sufficient to record the high level of cave surface detail. The data of the individual 47 scanning positions from the cave comprised almost 656 million points in total. Subsequent mutual registration of the scanning positions was processed in the RiSCAN PRO software by RIEGL using the iterative closest point adjustment of the consecutive scans termed Multi-Station Adjustment (MSA) (Ullrich et al., 2003). The resulting internal data registration error (standard deviation) of mutual orientation of all scans was 6.7 mm. Points captured within the manufacturer-defined minimum scanning range of 2.5 m from the scanner were removed from further processing due to the high probability of positional inaccuracy. For obtaining the intensity values corresponding with the surface reflectance only, points recorded with the full emitted pulse captured as a single echo were used. The points recorded as multiple echoes or stray points with a high pulse

shape deviation were filtered out. After registration and filtering, the final point cloud comprised 218,378,760 points with regular spacing set to 5 mm at a 10-meter range.

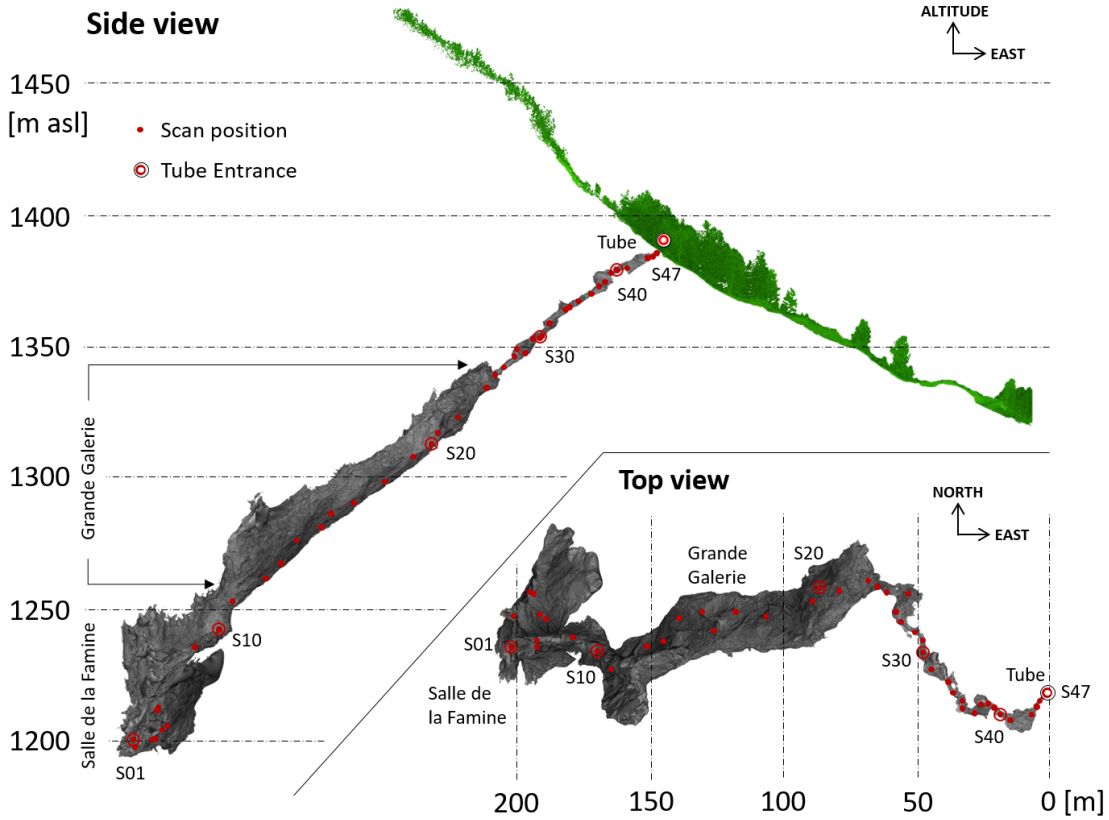

Fig. 3. The top view and side view of the laser-scanned part of Gouffre Georges comprising the domes of Salle de la Famine and Grande Galerie accessible via the Tube entrance with marked TLS positions (red dots) and cave exterior (green).

3.2. Intensity calibration experiment

Two sets of indoor experiments with different targets and varying acquisition geometry were conducted. The angular step width was set to Panorama 10 with an angular increment of 0.01° to ensure sufficient point density. The experimental settings are summarized in Tab. 2. The effect of distance on the recorded laser intensity was investigated by consecutive scanning of a white reference target with the size of 1 x 0.5 m mounted on a panel stand. Scanning started at the target´s position of 2.5 m away from the scanner with the next scanning position at the distance of 3 m from the device, and then each position with an increment of 1 m up to 60 m for the last position (Fig. 4). For each scan, the target was perpendicular to the scanner to eliminate the influence of the incidence angle. During

the data processing, the incidence angles were computed and only the data of incidence angle below 2° were kept. Points captured beyond the white reference target, including the panel stand, were removed.

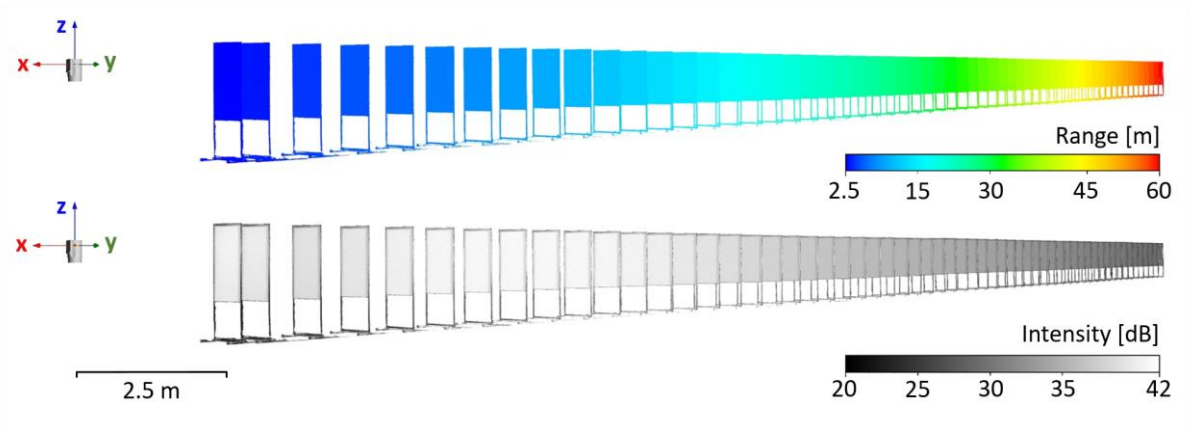

Fig. 4. Scene of the calibration experiment showing the position of the scanner with respect to the scanned white target for distances from 2.5 to 60 m. Recorded intensity decreases for longer ranges.

The second part of the experiment involved scanning samples of rocks collected from the cave during the TLS survey. Each sample of marble and lherzolite was fixed on a revolvable base on a tripod and scanned at a fixed distance of 5 m while varying the incidence angle. The initial 0° incidence angle was maintained by a perpendicular position to the scanner. The samples were rotated along their vertical axis by a 10° increment starting from 0° with respect to the scanner approaching 90° for the last scan. The data of different incidence angles required for further analysis were selected during the post-processing. Lastly, the samples were scanned from the 5 m distance and 0° incidence angle as dry samples. Afterward, the rocks were soaked in water for simulating condensation of air humidity on the rock surface in the cave environment and analysing its influence on the recorded intensity.

Tab. 2. Summary of the settings for the calibration experiments

	Range experiment	**Incidence angle experiment**
Scanned object	White reference target	Rock samples
Measurement program	Panorama 10	Panorama 10
Angular increment	0.01°	0.01°
Scanning range	2.5 – 60 m	5 m
Incidence angle	close to 0°	0° – close to 90°

3.3. Intensity correction

The character of the cave environment, especially the complex cave walls geometry and variable dimensions of the cave spaces can considerably influence the recorded intensity values. The temperature in a cave is influenced by the exchange of the cave air with the surface air, especially in passages near the entrance. Further in the cave, the temperature in most caves is close to the mean annual temperature of the region (James, 2013). The sensibility to temperature appears to be observable in the case of continuous-wave LiDAR instruments more than for the time-of-flight laser scanners. Errington and Daku (2017) have shown that the temperature compensation for radiometric correction is not necessary for the RIEGL device. However, a high concentration of particulates in the form of aerosol consisting of spores, dust, and water droplets is common in the cave, diminishing the laser pulse while propagating. The relative humidity varies depending on the vicinity of the entrance, ranging typically between 50 and 99 %. Deeper into the cave and further inside from the entrance, and where vadose seepage or flowing water is present, relative humidity is stable and close to 100 % (James, 2013). Under these circumstances, the atmospheric attenuation factor should be taken into consideration when laser intensity is to be corrected.

For analysing the corrected intensity values I_c proportional to the object surface reflectance $I_c \propto f(\rho_\lambda)$, other influencing factors should be eliminated. According to Equation (4) effects of the main physical parameters affecting the value of intensity can be described as a function of the surface reflectance $f(\rho_\lambda)$, distance effect $f_1(R)$, incidence angle $f_2(\alpha)$ and for the presented research with the inclusion of the atmospheric attenuation effect $f_3(\eta_{atm})$:

$$I = f(\rho_\lambda) * f_1(R) * f_2(\alpha) * f_3(\eta_{atm}) \quad \text{(Eq. 5)}$$

3.3.1. Correction of the distance effect

For the extended target, when the target is larger than the size of a laser footprint, so the entire energy of the laser footprint reflects on its surface, the backscattered signal power is inversely proportional to the squared range proceeding from the radar equation. However, the distance effect

is dependent on the instrumental properties and does not follow the $1/R^2$ relation for near distances less than 10 - 15 m varying for different laser scanners (Kaasalainen et al., 2011). The explanation for the near-distance effect links to the defocusing effect of the receiver´s optics (Fang et al., 2014). As the continuous function in a closed interval can be approximated by the polynomial series, the range function for the particular device can be data-driven from the reference measurements (Tan et al., 2016). Therefore, the function of the distance effect $f_1(R)$ for a specific instrument can be expressed as:

$$f_1(R) = \sum_{k=0}^{n} p_k R^k \quad \text{(Eq. 6)}$$

where p_k stands for the polynomial coefficients, which were estimated from the measured intensity of the reference target of the calibration experiment using least-squares adjustment.

3.3.2. Correction of the incidence angle effect

The incidence angle enclosed by the surface normal vector and the incident laser beam can be calculated from the measured point coordinates and the scanner position. Assuming the surface has perfect diffuse scattering characteristics (i.e., Lambertian surface), the backscattered intensity is directly proportional to the cosine of the incidence angle (Nayar et al., 1991; Rees, 2013; Xu et al., 2017). With increasing irregularities of the natural surfaces, the deviation from the Lambertian model increases. These surfaces can be modelled using Oren-Nayar model based on the bidirectional reflectance distribution function (Oren and Nayar 1995, 1994). The geometry of the natural surface is described as a set of micro-facets with different orientations, returning more light in the direction of the light source more than the surface following the Lambertian reflectance model. We used the Oren-Nayar reflectance model implemented by Carrea et al. (2016) for the correction of the incidence angle effect taking into account the microstructures as the surface roughness. As in TLS the incident and reflected laser beams are coincident, function using the Oren-Nayar model can be simplified as follows:

$$f_2(\alpha) = cos(\alpha)(A + B\, sin(\alpha)\, tan(\alpha)) \quad \text{(Eq. 7)}$$

$$A = 1 - 0.5\frac{\sigma_{slope}^2}{\sigma_{slope}^2 + 0.33} \qquad B = 0.45\frac{\sigma_{slope}^2}{\sigma_{slope}^2 + 0.09}$$

where coefficients in A and B were defined by Oren and Nayar (1995) and parameter σ_{slope} represents the standard deviation of slope angle distribution of the micro-facets. As σ_{slope} depends on the surface roughness only, it was estimated from the reference rock samples calibration experiment dataset of different incidence angles after correcting the distance effect, therefore the intensities were dependent primarily on the surface properties.

Since the scanned surface of the rock samples contained many irregularities causing deviations of the incidence angle, only sample points with the integer values starting from 0° with a 10° increment up to 80° and the last dataset containing points with a maximum incidence angle of 89° were selected for the σ_{slope} parameter estimation. Sampled dataset of the selected points was then repeatedly corrected for the incidence angle effect according to Equation (7) with the value of σ_{slope} from 0° to 90° with an increment interval of 1°. By comparing the corrected intensity data, the σ_{slope} can be found as the optimal value minimizing the differences between intensities of different incidence angles.

3.3.3. Correction of the atmospheric attenuation effect

The atmospheric attenuation effect represents the diminution of the laser pulse while propagating through the atmosphere. It is related to the average atmospheric conditions during scanning, e.g., humidity, ambient temperature, aerosol concentration, and it can be described as (Höfle and Pfeifer, 2007; Ding et al., 2013):

$$f_3(\eta_{atm}) = 10^{-2Ra/10000} \quad \text{(Eq. 8)}$$

where a is the atmospheric attenuation coefficient. The attenuation of laser power for the horizontal propagation can range from 0.2 dB/km for clear conditions, 3.9 dB/km for haze conditions (Jelalian, 1992) up to more than 300 dB/km in very thick fog (Kim et al., 2001). For modelling the atmospheric effect without detailed meteorological data, an approximated value has to be defined. The attenuation coefficient a was determined for the selected cave parts based on the overlapping

data of different scanning positions after correcting the data for distance (range) and incidence angle effects.

3.4. Denoising

After applying the intensity correction, all scanning positions were merged into a single point cloud and again spatially homogenized with a regular point spacing of 5 mm to remove duplicate points in the overlapping parts of several scanning positions. The corrected intensity of the final point cloud was smoothed and outliers of extreme intensity were removed to obtain the most satisfactory results for intensity interpretation. This was achieved by neighbourhood analysis within 100 nearest points surrounding a location. Given the recorded point density such a neighbourhood represents an area of about 5x5 cm. Denoising, data classification, and visualization were performed in the CloudCompare software (Girardeau-Montaut, 2020).

3.5. Point cloud classification and accuracy assessment

The corrected intensity of the denoised final point cloud was used to differentiate the lithology apparent on the cave surface. For this task, the points were classified using threshold values derived from the experimental rock samples scanning dataset after applying the intensity correction for the scanning geometry influence. The atmospheric attenuation effect was neglected as the experimental rock samples scanning was performed in laboratory conditions at a short scanning range. We used the standard deviation with respect to the mean value of corrected intensity to classify the points as marble or lherzolite. We also considered the assumption that the rock samples do not entirely represent the rock properties within the cave environment. Hence, after the denoising, threshold values were defined based on the entire TLS dataset. Using the histogram clustering, we calculated the histogram limits of the corrected intensity values to separate classes of marble and lherzolite. We have also tested the Otsu method for thresholding (Otsu, 1979) by using the R plugin autothresholdr (Nolan

et al., 2022) and the K-means clustering, to which it is supposed to be equivalent in the multilevel thresholding (Liu and Yu, 2009).

The accuracy of the point cloud classification was assessed by comparing with the photographs taken in the approachable part of the Grande Galerie dome, where it was possible to ensure sufficient light conditions. The photographs were spatially aligned to the intensity-corrected TLS point cloud in the Meshlab software (Cignoni et al., 2008) via raster registration using mutual correspondences. The points were assigned with the natural colour as RGB triplets and the outlines of the lherzolite and marble rock were identified by visual interpretation of the natural colour. The classification accuracy was assessed using a confusion matrix (Tab. 3). True positives (TP) refer to all coincidently identified marble points and true negative (TN) to all coincidently identified lherzolite points according to the RGB and corrected intensity values. False positives (FP) stand for all marble points falsely identified as lherzolite and false negatives (FN) denote all lherzolite points falsely identified as marble.

Tab. 3. Confusion matrix used for the classification accuracy assessment.

		Reference	
		Marble	Lherzolite
Predicted	Marble	TP	FP
	Lherzolite	FN	TN

To evaluate the spatial correspondence between the classification based on the referenced RGB values and corrected intensity values representing different rock types, three indices were calculated, including marble accuracy (recall), lherzolite accuracy (specificity), and overall accuracy defined as follows:

$$Marble\ accuracy = \frac{TP}{TP+FN} \quad \text{(Eq. 9)}$$

$$Lherzolite\ accuracy = \frac{TN}{TN+FP} \quad \text{(Eq. 10)}$$

$$Overall\ accuracy = \frac{(TP+TN)}{(TP+FP+FN+TN)} \quad \text{(Eq. 11)}$$

4. Results

4.1. Intensity correction

The final and unified single point cloud contains the corrected intensity values which resulted from applying the proposed approach. The originally recorded laser intensity was corrected individually for each of the 47 scans. First, the intensity data were corrected for the influence of the scanning range based on the polynomial model fitted to the acquired empirical relationship between range and mean intensity values from the calibration experiment (Fig. 5).

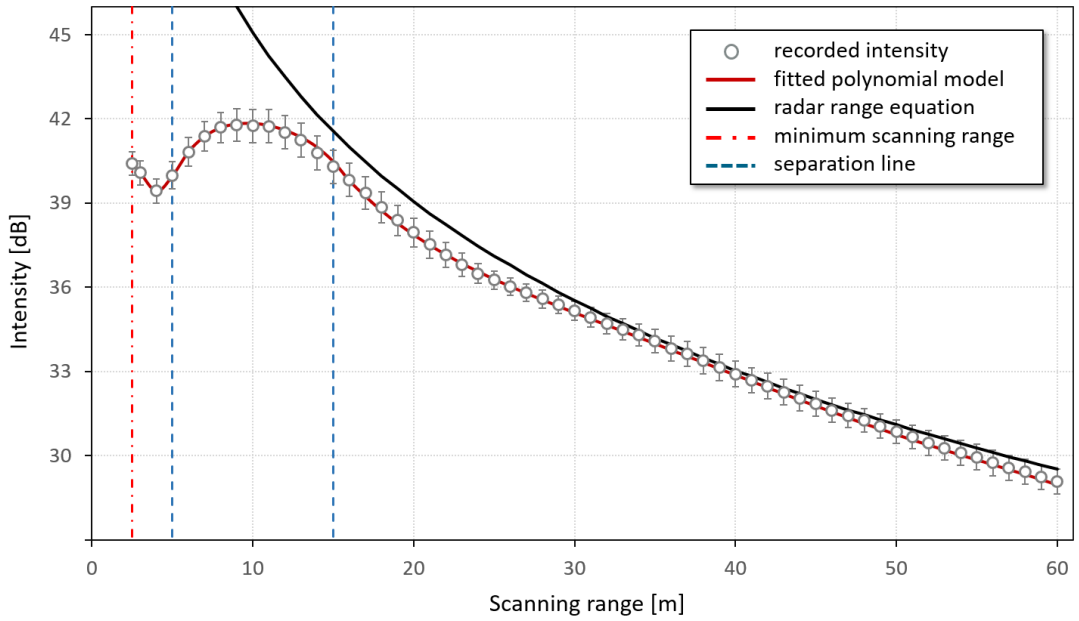

Fig. 5. Mean values of the recorded laser intensity of the reference target as the function of scanning range acquired by the RIEGL VZ-1000 in the laboratory experiment. The vertical bars show standard deviations of intensity measurements.

The relationship between scanning range and raw intensity recorded by RIEGL VZ-1000 markedly deviates from the radar range equation. Starting from the 2.5 m, declared as the minimum scanning range, intensity first rapidly decreases up to 4 m and then increases as a result of instrumental effect for the near distances. The peak is observed at the distance of around 10 m and then the recorded intensity values are considerably attenuated with the increasing range, approaching the radar equation function. To achieve a higher accuracy of fitting the model curve to the empirical data, we applied the piecewise fitting approach and divided the ranges into three intervals: below 5 m

comprising 4 data points including the local minimum, 5 - 15 m, and above 15 m. The derived polynomial coefficients are reported in Tab. 4.

Tab. 4. Polynomial coefficients used for the distance correction.

Range	p_0	p_1	p_2	p_3	p_4	p_5
R < 5 m	34.877	6.406	-2.279	0.241	-	-
5 - 15 m	27.106	4.725	-0.569	3.1361×10^{-2}	-7.016×10^{-4}	-
R > 15 m	64.714	-3.287	0.154	-3.808×10^{-3}	4.594×10^{-5}	-2.158×10^{-7}

For correction of the incidence angle effect, parameter σ_{slope} was estimated from the rock samples intensity data after applying the proposed distance effect correction. Subsequently, the incidence angle correction was applied on the sample dataset of different incidence angles according to Equation (7) with the varying σ_{slope} in the interval from 0° to 90°. Fig. 6 shows differences between mean corrected intensity values of incidence angle in the interval of 0 - 10° and the entire range of 0° to 89° for lherzolite and marble samples. The lowest variation of intensities of 0.0154 [dB] for marble was observed for σ_{slope} of 27° and 0.0083 [dB] for lherzolite at σ_{slope} of 31°. The mean σ_{slope} value of 29° was determined as the optimal value minimizing the variation of corrected intensity values of the observed incidence angles for both materials.

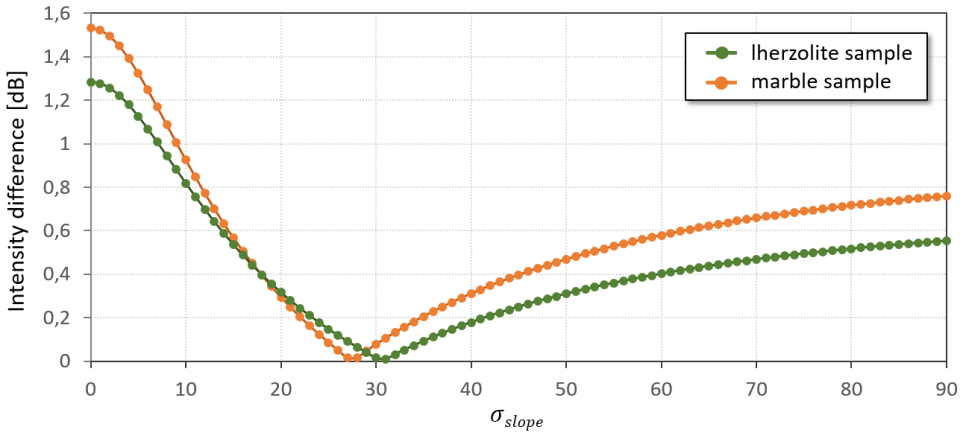

Fig. 6. Differences between intensity values of various incidence angles corrected using different σ_{slope} values for lherzolite and marble samples.

Determination of the σ_{slope} parameter for each material might improve the results of the intensity correction, however, the implementation is unfeasible without prior material differentiation within the entire dataset. Even a single optimized parameter significantly reduces the overcorrection of the high incidence effect for the rock surfaces with non-Lambertian behaviour (Carrea et al., 2016). Therefore a single σ_{slope} value of 29° was determined to be applicable for the entire Gouffre Georges data set minimizing the incidence angle effect.

After applying the primary correction to eliminate the influencing factors related to the scanning geometry on each of 47 cave scans, differences of the intensity values were observed in the overlapping parts of the scans, attributed to the energy loss due to the atmospheric conditions. Fig. 7 and Tab. 5 demonstrate this problem on a representative dataset of 3 overlapping scans of a wall comprising of marble in the Salle de la Famine dome acquired within distances of 21.5, 32.9, and 41.1 m.

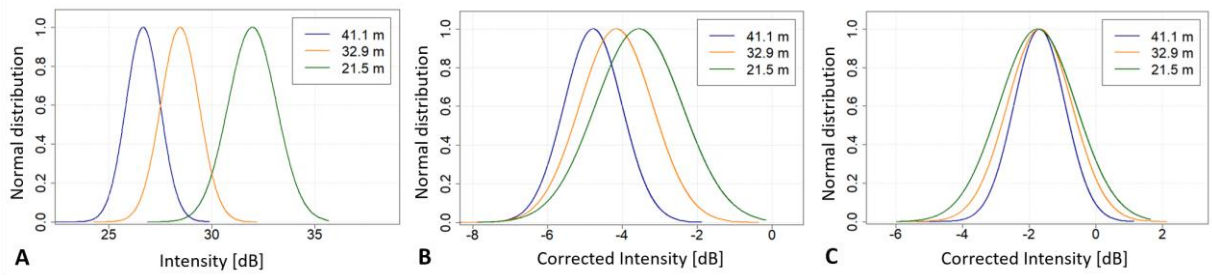

Fig. 7. Distribution of laser intensity data recorded from three overlapping scanning positions, i.e., three different ranges (41.1 m, 32.9 m, 21.5 m) capturing the same cave wall in the Salle de la Famine dome: (A) raw intensities, (B) intensities after the correction for distance and incidence angle, (C) final intensity values after the correction for the atmospheric attenuation.

Tab. 5. Summary statistics of the intensity distribution presented in Fig. 7: (A) raw intensities, (B) intensities after the correction for distance and incidence angle, (C) final intensity values after the correction for the atmospheric attenuation. The low index values refer to the scanning ranges as in Fig. 7.

	$A_{41.1}$	$A_{32.9}$	$A_{21.5}$	$B_{41.1}$	$B_{32.9}$	$B_{21.5}$	$C_{41.1}$	$C_{32.9}$	$C_{21.5}$
Minimum	22.360	24.240	26.850	-9.070	-8.303	-7.887	-5.920	-5.813	-5.999
Maximum	29.860	32.200	35.670	-1.880	-0.364	-0.162	1.143	2.128	1.648
Range	7.500	7.960	8.820	7.190	7.939	7.726	7.063	7.940	7.647
Mean	26.660	28.450	31.970	-4.782	-4.163	-3.556	-1.681	-1.679	-1.743
Std	0.832	0.929	1.175	0.777	0.978	1.163	0.771	0.975	1.158
1st quartile	26.180	27.900	31.280	-5.234	-4.756	-4.277	-2.128	-2.272	-2.468
Median	26.740	28.510	32.030	-4.718	-4.075	-3.459	-1.616	-1.591	-1.642
3rd quartile	27.230	29.120	32.780	-4.255	-3.481	-2.725	-1.154	-0.996	-0.920

The three curves of raw intensity distribution do not match and the highest intensity occurs at the shortest range and vice-versa (Fig. 7A). After the corrections for distance and incidence angle effect, the differences between the distribution curves are reduced although the range dependence is still apparent (Fig. 7B). The reason is in the energy loss of a laser pulse due to the atmospheric attenuation with increasing distance from the scanner. The atmospheric attenuation coefficient was determined for the particular cave sections based on selected small areas of overlapping data with consistent intensities at each scanning position. That prevented the confusion of diverse intensity values caused by the atmospheric attenuation with the influence of the different surface materials. Depending on the distance to the cave entrance or the waterflow, the coefficient of the atmospheric attenuation a varied for the selected overlaps of scans from 0.7 at 10 m to 1.8 dB for the maximal scanning ranges of 60 m. After correcting the atmospheric effect according to Equation (8), the intensity values at the overlapping scanning positions of different scanning ranges became very similar (Fig. 7C). We conducted the Kruskal-Wallis rank sum test to ascertain whether the three sample groups within the batch A, B, C are significantly different at p=0.01. This test was preferred from analysis of variance test

as the residuals of some sample groups were not normally distributed according to the Shapiro-Wilks tests and quantile-quantile plots. The results are reported in Tab. 6. The resulting p-value increases from A to C sample group and it is higher than the significance p=0.01 for the batch C. This supports the statistically significant similarity of the three groups in batch C.

Tab. 6. Results of the Kruskal-Wallis rank sum test of sample groups within the batches A (raw intensity), B (distance and incidence angle corrected), C (atmospheric attenuation corrected).

Sample groups	chi-sq	Degree of freedom	p-value
$A_{44.1}$			
$A_{32.9}$	14.013	2	0.000906
$A_{21.5}$			
$B_{44.1}$			
$B_{32.9}$	11.942	2	0.002552
$B_{21.5}$			
$C_{44.1}$			
$C_{32.9}$	9.0364	2	0.010912
$C_{21.5}$			

The range dependence of the original raw intensity values is most evident when combining the individual scanning positions (Fig. 8A, 8B). Data shadows occurred primarily in the most constricted parts and also in vertical transitions, where stabilization of the scanning positions was difficult. In this case, no 3D surface model was interpolated from the TLS data. Even though it would interpolate points in the areas of evident data shadows, it would also distort the resulting interpretation of real recorded intensity values and the mapped objects. In the narrow passage leading from the Tube entrance down to the Grande Galerie dome, the data scanned closer to the scanner than the recommended minimum scanning range of 2.5 m were kept for visualization purposes. In these confined cave sections, the TLS captured points at a distance of ca. 0.9 m, but with a certain position inaccuracy. Therefore, the further results on the interpretation of the corrected intensity data concern the large domes of Grande Galerie and Salle de la Famine.

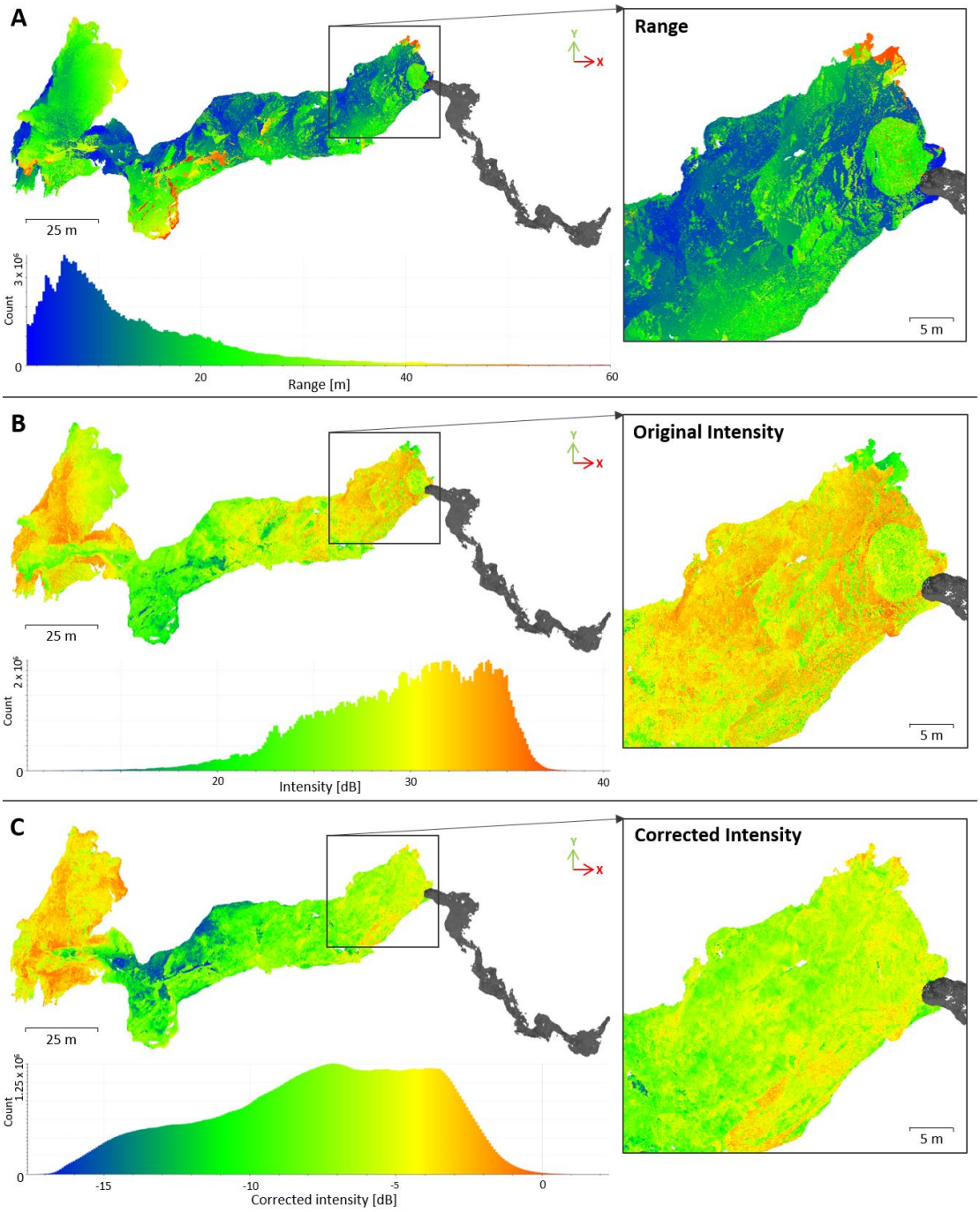

494

495 Fig. 8. Final point cloud comprising of 47 scanning positions coloured by the (A) range values (B) original intensity (C)

496 corrected intensity.

497 The original intensity data of each scanning position rapidly decreases with the longer scanning

498 ranges and the highest intensity values are primarily near the centre of the scanned point cloud (Fig.

499 8B). Merging these datasets into a single point cloud without any correction would lead to the

500 misinterpretation of the surface materials. After eliminating the distance, incidence angle, and

atmospheric attenuation effects, the resulting corrected intensity values depend primarily on the surface material. Even though data before applying the correction indicates different materials, acquired corrected intensity values delimited material borders and sections with water occurrence and the watercourse in the lower part of the Grande Galerie dome. Areas in the vicinity of the watercourse evince the lowest intensity values as a consequence of the water droplets. Similarly, the histogram distribution of the corrected intensity indicates the presence of three main different types of surface materials.

By applying the denoising process of nearest neighbour analysis, outliers comprising 0.015% points were removed from the entire dataset. After this step, the histogram distribution is also more delimited representing intensity limits for the different types of materials (Fig. 9). Although smoothing may increase the uncertainty of the boundary position between the observed rocks by its shifting in the direction of the prevailing values, it allows better distinguishing of the significant areas of different rock types contact. One of these most noticeable features, the significant contact of lherzolite and marble is visible in the upper part of the Grande Galerie dome. The indicator of this strong contrast was visually recognizable from the original intensity values. However, the influence of the distance effect is apparent resulting in the intensity values decrease with increasing range for the displayed scanning positions acquired from about 20, 40, and 55 metres described within the upper right scatterplot of the originally recorded intensity (Fig. 9A). After the intensity correction, the dependence on distance is eliminated and the boundaries are clearly demarcated, the overlapping data of different ranges evince similar intensity values (Fig. 9B). The distribution indicates two distinct materials in the scatterplot of corrected intensity values with dashed line representing the boundary between them. For high point density of each scanning position, the points are expressed by values of the probability density function (PDF).

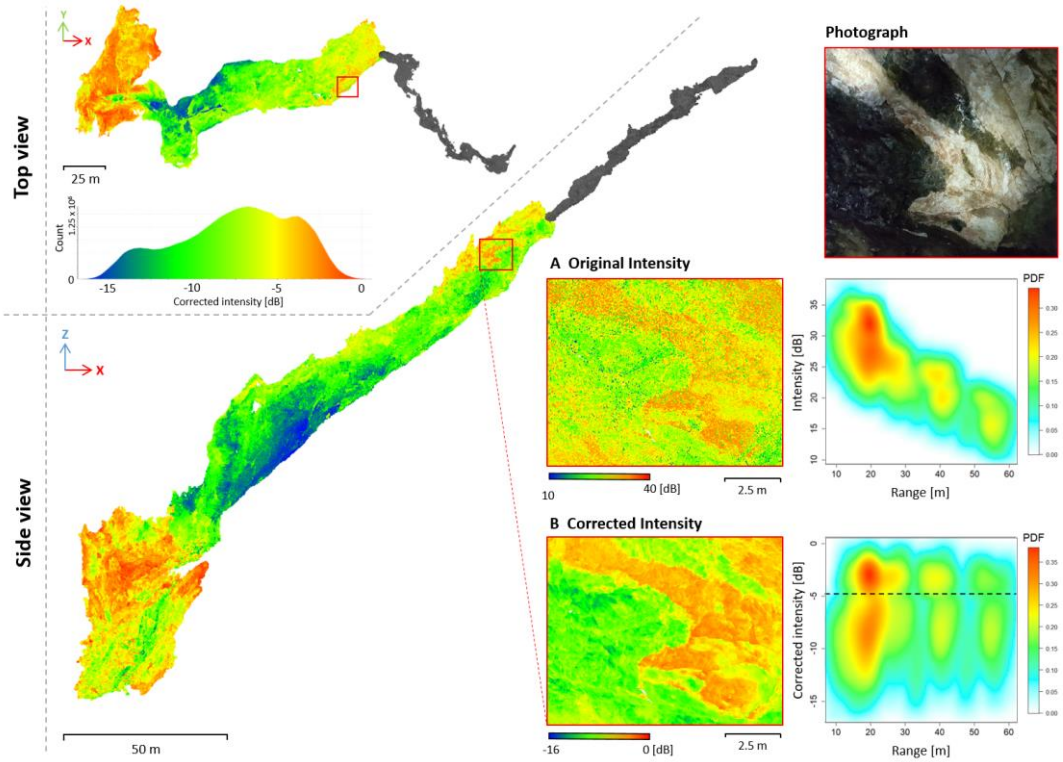

524

525 Fig. 9. Top and side view of the selected Gouffre Georges cave parts point cloud with corrected intensity values after removing
526 the outliers by the denoising, revealing the lithological contacts and the strong water occurrence. The dashed line in the
527 scatterplot indicates the boundary between marble and lherzolite.

528

529 **4.2. Lithological differentiation based on the corrected laser intensity**

530 The primary lithological differentiation was performed by classifying the 3D point cloud based on
531 the determined intensity intervals for the observed materials. The first classification approach was
532 based on the thresholds defined by the mean and standard deviation of the corrected intensities of
533 the rock samples (Tab. 7), thus derived in the lab experiment. Moistening the rock samples surfaces
534 caused a shift towards lower intensity values for both rock types as a result of absorbing the near-
535 infrared wavelengths by the water (Fig. 10).

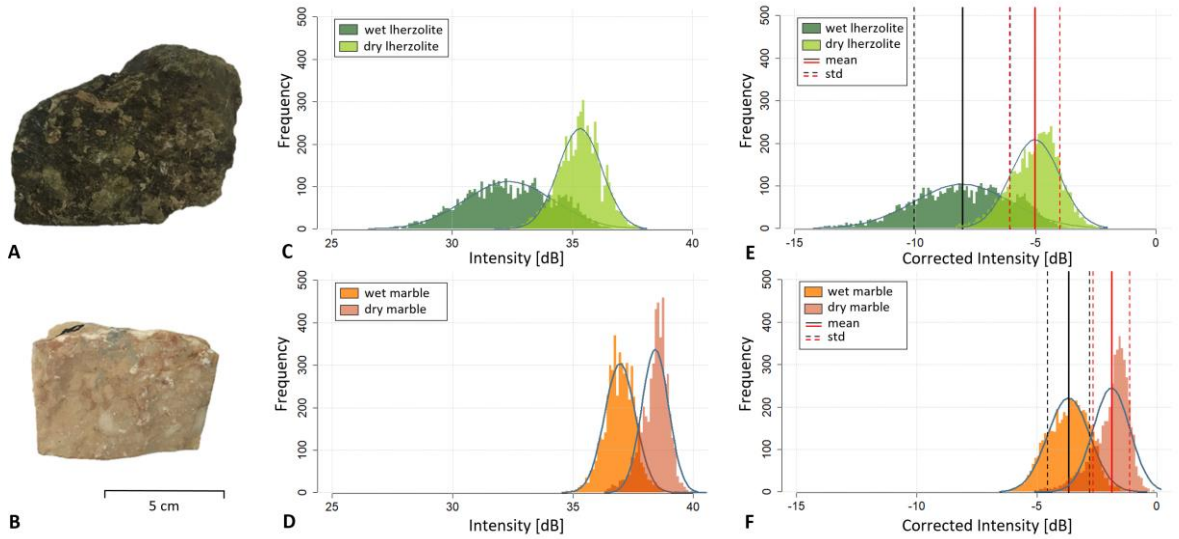

Fig. 10. Results of scanning of the (A) lherzolite and (B) marble samples: distribution of the original intensities for the samples of (C) lherzolite and (D) marble, and the distribution of the corrected intensities for the samples of (E) lherzolite and (F) marble, each observed under the dry and wet surface conditions. The blue bell-shaped curve indicates normal distribution model based on the sample mean and standard deviation as reported in Tab. 7 and vertical dashed and solid lines, respectively.

Tab. 7. Mean and standard deviation of the corrected intensity values of the scanned rock samples.

Sample	Condition	Mean	Std
Lherzolite	wet	-8.043	1.995
	dry	-5.036	1.022
Marble	wet	-3.676	0.875
	dry	-1.895	0.763

The intensity values of lherzolite decreased on average by 3 dB and marble by 1.8 dB, while the decrease in the surface reflectivity represents almost 13 % for lherzolite and 22 % for marble. Different rate of decline is related to the amount of applied water, the rock properties, and its ability to absorb the water. The laser intensities of the samples for both rock types remained distinguishable for both wet and dry conditions after the intensity correction. Tab. 8 reports the statistics of Welch Two sample t-test with null hypothesis that the two samples are not significantly different at p=0.01. Results of all four combinations allow for accepting the statistically significant difference between the wet and dry

552 samples of the two rock types. Therefore, we could further use the corrected intensity values for
553 differentiating the lherzolite and marble even in the cave environment.

554 Tab. 8. Results of Welch Two Sample t-test of difference between corrected laser intensities of wet and dry samples of
555 lherzolite and marble.

556

Combination of two samples	t-value	Degrees of freedom	p-value
Lherzolite dry and lherzolite wet	-97.072	7723	< 2.2e-16
Marble dry and marble wet	-106.10	9465	< 2.2e-16
Lerzolite dry and marble dry	-175.66	9796	< 2.2e-16
Lherzolite wet and marble wet	-143.83	7250	< 2.2e-16
Lherzolite dry and marble wet	-72.359	10179	< 2.2e-16
Lherzolite wet and marble dry	-206.26	6841	< 2.2e-16

557
558
559
560
561

562 The threshold intensities were determined independently of the surface wetness conditions to
563 classify the LiDAR points into the two rock classes within the cave environment. The intensity limit was
564 set from -10.038 to -4.014 dB and -4.551 to -1.132 dB, for lherzolite and marble respectively. The points
565 with intensities below the lower threshold of lherzolite (-10.038 dB) were considered as strongly
566 influenced by the presence of water as their intensity values were similar to the values in the lower
567 part of Grande Galerie with the watercourse. Hence, the points were assigned to the class of water
568 (Fig. 9C). With the slight overlap of the lower-intensity threshold for the wet marble and the upper-
569 intensity threshold of the dry lherzolite, a misinterpretation of the surface materials is expected for
570 5.14 % of points from the entire dataset. The second classification approach used the intensity limits
571 determined from the histogram distribution of the corrected intensity values of the entire final point
572 cloud (Fig. 9), thus derived from recordings from the natural cave environment. The threshold of -4.783
573 dB was used to distinguish lherzolite and marble and -12.207 dB was applied to separate lherzolite
574 from water class. The other approaches also proceeded from the entire cave point cloud. The third
575 classification used the Otsu method to define the threshold of -6.736 dB between marble and lherzolite
576 after removing the water class based on the previous limit. And the fourth classification method, K-

means clustering, determined the threshold of -5.996 dB between marble and lherzolite and -10.231 dB between lherzolite and the water class.

The classification assessment is presented on the example of the upper part of Grande Galerie, where there is no presumable strong water occurrence, on a wall with no present mud and flowstone coverage (Fig. 9, Fig. 11A). The assessment of the classification accuracy was performed on the selected point cloud containing over 1.896 million points with assigned RGB values and three classes determined from the lab and the cave environment data. As the water occurrence is not recognizable from the RGB information, the points representing this class identified by all approaches were not included in the assessment. This class comprised 108,380 points (5.71 %) based on the first approach and 5,105 points (0.26 %) based on the second and third classification approach and 89,493 points (4.72 %) based on the fourth classification method. Tab. 9 reports the calculated classification accuracy with the measures defined in Section 3.5. For all approaches, the overall accuracy is high (over 84 %). The most successful results with highest overall accuracy was achieved by using the second approach for which the intensity limits were determined from the point cloud histogram distribution of the corrected intensity values.

Tab. 9. Classification accuracy of the four approaches based on the lab-recorded intensity (Classification 1), the thresholds from the histogram distribution of the corrected intensity of the cave point cloud (Classification 2), the Otsu thresholding (Classification 3), the K-means clustering (Classification 4).

	Marble Accuracy	**Lherzolite Accuracy**	**Overall Accuracy**
Classification 1	97.96 %	80.90 %	86.18 %
Classification 2	95.19 %	85.47 %	89.24 %
Classification 3	74.51 %	97.41 %	84.03 %
Classification 4	82.90%	95.52 %	88.73 %

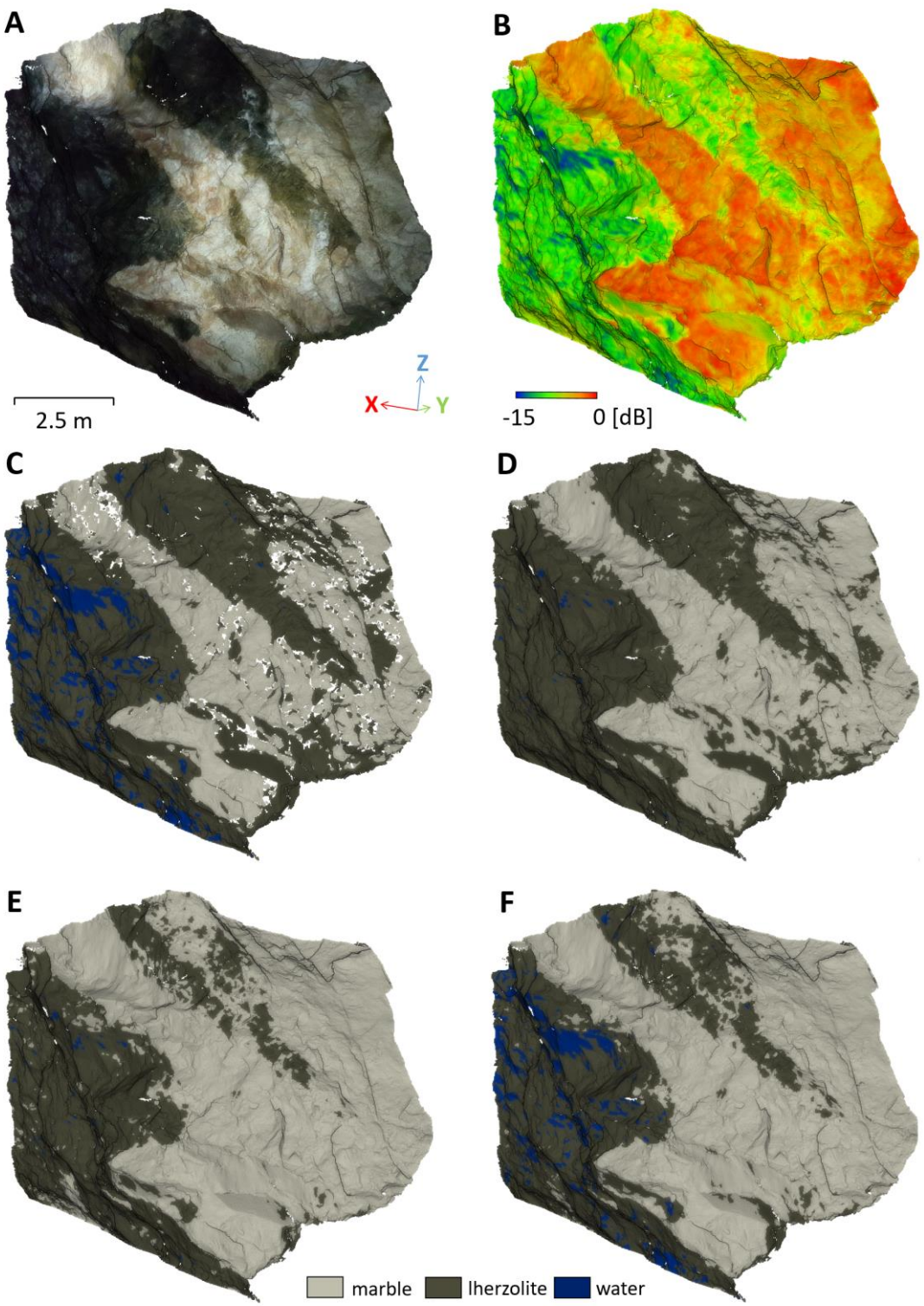

Fig. 11. Section of the 3D TLS point cloud from Grande Galerie (Fig. 9) comprising a cave wall coloured by (A) photographed natural colours with dark lherzolite and light marble, (B) the corrected intensity values, (C) classification based on the thresholds from corrected intensities of the rock samples, (D) classification based on the thresholds from the histogram of the corrected intensity of the cave, (E) classification based on the Otsu thresholding, and (F) classification based on the K-means clustering.

602 The classification results for the entire cave environment are presented for the most successful
603 classification approach based on the histogram clustering. Proceeding from the histogram distribution
604 of the corrected intensity values, marble represents 24.49 %, lherzolite 63.43 %, and water 12.08 % of
605 points in the analysed dataset. The classification was focused on the three, most dominant classes, not
606 considering other surface materials or surface changes. As it was applied on the entire cave dataset
607 including the cave floor, the occurrence of mud is presumable. The problematic are also the areas in
608 the vicinity of the watercourse, which evince the lowest intensity values as a consequence of the water
609 droplets. The strong water occurrence near the water course or in a form of condensed water mainly
610 on the ceiling could significantly influence the intensity values and subsequent material differentiation.
611 This can be partially solved by the local histogram clustering applied on the selected cave sections.
612 After segmenting the cave to the central part strongly influenced by water and parts with minimum
613 water occurrence during the data acquisition, i.e., Salle de la Famine dome and the upper part of the
614 Grande Galerie or even smaller section, e.g., ceiling or cave floor to discriminate the scree material,
615 the threshold values for the cave section with strong water occurrence were defined individually based
616 on the repeated histogram clustering. After combining all of these segments, the cave point cloud
617 comprises 59.11 % marble, 40.42 % lherzolite, and only 0.47 % of points were assigned as water (Fig.
618 12). The water occurrence caused the decrease of the intensity values of 3 to almost 5 dB, therefore
619 the marble in some section was assigned as lherzolite and lherzolite was classified as water.

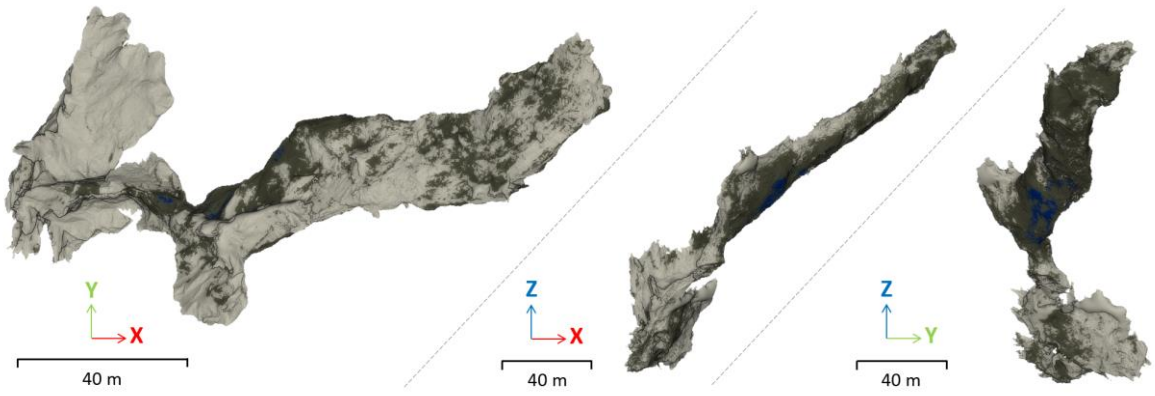

620

621 Fig. 12. Results of the material differentiation based on the histogram clustering applied individually on the segmented cave
622 sections.

5. Discussion

Results of the range calibration experiment performed with a reference target evinced that the TLS recorded intensity values are not inversely proportional to the squared value of range, especially at near distances. This relationship may even vary for different TLS devices. The range dependence is also present for the attenuation effect, which is besides the scanning range influenced by the vicinity of the entrance or waterflow. Therefore, the irregular morphology and cave variable dimensions captured by multiple scanning positions determine the need for a complex intensity correction approach. Our results also show that TLS intensity data is applicable for distinguishing the rock material of the scanned surface in the cave environment. Laser scanning of the cave thus provides a highly detailed perception of the 3D geometry and also information about the properties of the rock surface.

The data acquired by the one-wavelength LiDAR instrument may be limited due to the restricted spectral information. Overlapping intensity distributions of mapped rock types restrict the material differentiation (Matasci et al., 2015). Marble and lherzolite evince distinct reflectances at 1,550 nm enabling the lithological classification using the presented approach. Rock types with small spectral differences at one wavelength can be distinguished based on the spectral information from different channels (Kaasalainen and Malkamäki, 2020; Chen et al., 2018). However, multi-wavelength TLS instrument is not commercially available yet.

Recent studies demonstrated the applicability of digital photogrammetry for acquiring 3D cave datasets for analysis of morphologies and geological structures, using a digital camera for ground-captured photographs (De Waele et al., 2018) or combined with an unmanned aerial vehicle (UAV) (Triantafyllou et al., 2019). Also, a combination of digital photogrammetry and laser scanning was successfully used in a cave to reveal painted black rock art behind graffiti and moss (Jalandoni et al., 2021). The cave dimensions and primarily the light conditions in the cave are the main limiting factor of applying passive remote sensing. Artificial illumination must be used either in the form of a flashlight on the camera or spotlights in the scene. Also, the irregularity and complexness of cave morphology introduce shadows and overexposure, resulting in low-quality 3D model reconstruction. The exposure

649 variation can lead to the incorrect differentiation of materials and can be problematic for further
650 analysis and interpretation of lithology. The extent of cave space in Gouffre Georges was in the order
651 of tens and hundreds of meters which is too large to ensure optimum illumination. In the abseiling
652 parts, the use of photography is hardly possible.

653 Material differentiation and classification of the point cloud to map not only the observed
654 lherzolite and marble based on the corrected intensity has some limitations. The presence of water
655 considerably affects the discrimination of mapped materials as the moisture content causes decrease
656 of the intensity values. The water occurrence covering the rocks in the close vicinity of the watercourse
657 complicates the material differentiation based on the corrected intensity in the lower part of the
658 Grande Galerie. Consequently, in these parts of the cave, the determined threshold values of corrected
659 intensity for marble can be assigned as lherzolite. This fact indicates the limitation of using of the
660 corrected intensity for the material differentiation in the water course surroundings or places of
661 significant water seepage characteristic for the cave environment. Therefore, it is necessary to map
662 and interpret the wet parts as well as in case of the flowstone or mud occurrence in the cave
663 individually and use supplementing data sources and field measurements. The results of the LiDAR
664 survey in the Gouffre Georges cave show that intensity data, albeit a by-product of the survey and
665 acquired 3D geometry, provide valuable information for detailed mapping of rock types in
666 underground environments.

667 ## 6. Conclusion

668 The presented case study in Gouffre Georges demonstrated an efficient and complex intensity
669 correction procedure for data acquired in the cave environment for mapping the surface material. The
670 key step in this approach is the elimination of the influencing factors related to the scanning geometry,
671 surface roughness, and atmospheric attenuation. Such conditions have to be considered before
672 applying the recorded laser intensity to mapping.

The geological and lithological setting of the Gouffre Georges is rather unique in the whole Pyrenean belt since it allows to observe with a spectacular continuity and without any vegetal cover the contact between marble and lherzolite. The laser scanning of the cave geometry assigned with the corrected laser intensity is an invaluable tool to unravel the complexity of such a lithological environment. This work contributes to the growing body of studies demonstrating the potential of LiDAR remote sensing even in the underground environment by showing that it has the potential to differentiate material using laser intensity data. Furthermore, the presented approach is transposable to artificial underground spaces, such as tunnels, cellars, or mining shafts, which are similar to caves in terms of environmental conditions.

Acknowledgement

The presented research was financially supported by the Ministry of Education, Science, Research and Sport of the Slovak Republic under the grant nr. VEGA 1/0798/20 “Synergistic use of multiple remote sensing data sources in geographic research” and VEGA 1/0168/22 “Paleogeographic and geodynamic interpretations of detrital minerals from selected areas of the Western Carpathians: a case study identifying the nature of transport conditions and source areas in karst and non-karst areas”. Riccardo Asti wishes to acknowledge the Orogen Project (BRGM, Total, CNRS-INSU) for providing a post-doc grant. Yves Lagabrielle is warmly thanked for helping the scientific organization of the expedition in the cave. Nicolas Clément, Robert Guinot and the SCHS (Spéléo Club du Haut Sabarthez) speleological club of Tarascon-sur-Ariège are greatly thanked for their support during the acquisition days. We highly appreciate the comments and suggestions of the reviewers which contributed to the improved presentation of the conducted research.

References

Angrand P, Mouthereau F, Masini E, Asti R., 2020. A reconstruction of Iberia accounting for W-Tethys/N-Atlantic kinematics since the late Permian-Triassic. Solid Earth. https://doi.org/10.5194/se-2020-24.

Asti, R., Lagabrielle, Y., Fourcade, S., Corre, B., Monié, P., 2019. How do continents deform during mantle exhumation? Insights from the northern Iberia inverted paleopassive margin, western Pyrenees (France). Tectonics, 38, 1666–1693. https://doi.org/10.1029/2018TC005428.

Azmy, S. N., Sah, S. A. M., Shafie, N. J., Ariffin, A., Majid, Z., Ismail, M. N. A., Shamsir, M. S., 2012. Counting in the dark: non-intrusive laser scanning for population counting and identifying roosting bats. Scientific Reports, 2, 524. https://doi.org/10.1038/srep00524.

Berenguer-Sempere, F., Gómez-Lende, M., Seranno, E., de Sanjosé-Blasco, J. J., 2014. Orthothermographies and 3D modeling as potential tools in ice caves studies: the Peña Castil Ice Cave (Picos de Europa, Northern Spain). International Journal of Speleology, 43(1), 4. https://doi.org/10.5038/1827-806X.43.1.4.

Burens, A., Grussenmeyer, P., Guillemin, S., Carozza, L., Lévêque, F., and Mathé, V., 2013. Methodological developments in 3D scanning and modelling of archaeological French heritage site: the Bronze Age painted cave of "Les Fraux", Dordogne (France), Int. Arch. Photogramm. Remote Sens. Spatial Inf. Sci., XL-5/W2, 131–135. https://doi.org/10.5194/isprsarchives-XL-5-W2-131-2013.

Carrea, D., Abellan, A., Humair, F., Matasci, B., Derron, M. H., Jaboyedoff, M., 2016. Correction of terrestrial LiDAR intensity channel using Oren–Nayar reflectance model: An application to lithological differentiation. ISPRS Journal of Photogrammetry and Remote Sensing, 113, 17-29. https://doi.org/10.1016/j.isprsjprs.2015.12.004.

Chen, Y., Jiang, C., Hyyppä, J., Qiu, S., Wang, Z., Tian, M., Puttonen, E., Zhou, H, Feng, Z., Bo, Y., Wen, Z., 2018. Feasibility study of ore classification using active hyperspectral LiDAR. IEEE Geoscience and Remote Sensing Letters, 15(11), 1785-1789. https://doi.org/10.1109/LGRS.2018.2854358

Cignoni, P., Callieri, M. , Corsini, M., Dellepiane, M., Ganovelli, F., Ranzuglia, G., 2008. MeshLab: an Open-Source Mesh Processing Tool. Sixth Eurographics Italian Chapter Conference, pp. 129-136.

Clerc C, Lagabrielle, Y., Neumaier M., Reynaud J.-Y., de Saint Blanquat M., 2012. Exhumation of subcontinental mantle rocks: evidence from ultramafic-bearing clatic deposits nearby the Lherz peridotite body, French Pyrenees. Bulletin de la Société géologique de France, 183(5), 443-459. https://doi.org/10.2113/gssgfbull.183.5.443.

Clerc, C., Lagabrielle, Y., 2014. Thermal control on the modes of crustal thinning leading to mantle exhumation: Insights from the Cretaceous Pyrenean hot paleomargins. Tectonics, 33, 1340–1359. https://doi.org/10.1002/2013TC003471.

Clerc, C., Lahfid, A., Monié, P., Lagabrielle, Y., Chopin, C., Poujol, M., Boulvais, J., Ringenbach, C., Masini, E., de St Blanquat, M., 2015. High-temperature metamorphism during extreme thinning of the continental crust: A reappraisal of the north Pyrenean passive paleomargin. Solid Earth, 6(2), 643–668. https://doi.org/10.5194/se-6-643-2015.

Cosso, T., Ferrando, I., Orlando, A., 2014. Surveying and mapping a cave using 3d laser scanner: the open challenge with free and open source software. International Archives of the Photogrammetry, Remote Sensing & Spatial Information Sciences, 45. https://doi.org/10.5194/isprsarchives-XL-5-181-2014.

Debroas, E. J., Canérot, J., Bilotte, M., 2010. Les Brèches d'Urdach, témoins de l'exhumation du manteau pyrénéen dans un escarpement de faille Vraconnien-Cénomanien inférieur (zone nord-pyrénéenne, Pyrénées-Atlantiques, France). Géologie de la France, 2, 53–63.

De Waele, J., Fabbri, S., Santagata, T., Chiarini, V., Columbu, A., Pisani, L., 2018. Geomorphological and speleogenetical observations using terrestrial laser scanning and 3D photogrammetry in a gypsum cave (Emilia Romagna, N. Italy). Geomorphology, 319, 47-61. https://doi.org/10.1016/j.geomorph.2018.07.012.

Ding, Q., Chen, W., King, B., Liu, Y., Liu, G., 2013. Combination of overlap-driven adjustment and Phong model for LiDAR intensity correction. ISPRS journal of photogrammetry and remote sensing, 75, 40-47. https://doi.org/10.1016/j.isprsjprs.2012.09.015.

Ducoux, M., Jolivet, L., Callot, J. P., Aubourg, C., Masini, E., Lahfid, A., Homonnay, E., Cagnard, F., Gumiaux., C., Baudin, T., 2019. The Nappe des Marbres unit of the Basque-Cantabrian Basin: the tectono-thermal evolution of a fossil hyperextended rift basin. Tectonics, 38(11), 3881-3915. https://doi.org/10.1029/2018TC005348.

Duretz, T., Asti, R., Lagabrielle, Y., Brun, J.P., Jourdon, A., Clerc, C., Corre, B., 2019. Numerical modelling of syn-rift salt tectonics during Cretaceous Pyrenean Rifting. Basin Research, 32(4), 652-667. https://doi.org/10.1111/bre.12389.

Eitel, J. U., Höfle, B., Vierling, L. A., Abellán, A., Asner, G. P., Deems, J. S., Glennie, C. L., Joerg, P. C., LeWinter, A. L., Magney, T. S., Mandlburger, G., Morton, D. C., Müller, J., Vierling, K. T., 2016. Beyond 3-D: The new spectrum of lidar applications for earth and ecological sciences. Remote Sensing of Environment, 186, 372-392. https://doi.org/10.1016/j.rse.2016.08.018.

Errington, A. F., Daku, B. L., 2017. Temperature compensation for radiometric correction of terrestrial LiDAR intensity data. Remote Sensing, 9(4), 356. https://doi.org/10.3390/rs9040356.

Fabbri, S., Sauro, F., Santagata, T., Rossi, G., De Waele, J., 2017. High-resolution 3-D mapping using terrestrial laser scanning as a tool for geomorphological and speleogenetical studies in caves: An example from the Lessini mountains (North Italy). Geomorphology, 280, 16-29. https://doi.org/10.1016/j.geomorph.2016.12.001.

Fang, W., Huang, X., Zhang, F., Li, D., 2014. Intensity correction of terrestrial laser scanning data by estimating laser transmission function. IEEE Transactions on Geoscience and Remote Sensing, 53(2), 942-951. https://doi.org/10.1109/TGRS.2014.2330852.

Franceschi, M., Teza, G., Preto, N., Pesci, A., Galgaro, A., Girardi, S., 2009. Discrimination between marls and limestones using intensity data from terrestrial laser scanner. ISPRS Journal of Photogrammetry and remote sensing, 64(6), 522-528. https://doi.org/10.1016/j.isprsjprs.2009.03.003.

Gallay, M., Kaňuk, J., Hochmuth, Z., Meneely, J. D., Hofierka, J., Sedlák, V., 2015. Large-scale and high-resolution 3-D cave mapping by terrestrial laser scanning: a case study of the Domica Cave, Slovakia. International Journal of Speleology, 44(3), 6. http://doi.org/10.5038/1827-806X.44.3.6.

Gallay, M., Hochmuth, Z., Kaňuk, J., Hofierka, J., 2016. Geomorphometric analysis of cave ceiling channels mapped with 3-D terrestrial laser scanning. Hydrology and Earth System Sciences, 20(5), 1827. https://doi.org/10.5194/hess-20-1827-2016.

Guha, A., Ghosh, B., Kumar, K. V., Chaudhury, S., 2015. Implementation of reflection spectroscopy based new ASTER indices and principal components to delineate chromitite and associated ultramafic–mafic complex in parts of Dharwar Craton, India. Advances in Space Research, 56(7), 1453-1468. https://doi.org/10.1016/j.asr.2015.06.043.

Girardeau-Montaut, D., 2020. CloudCompare – 3D point cloud and mesh processing software. Open Source Project.

Höfle, B., Pfeifer, N., 2007. Correction of laser scanning intensity data: Data and model-driven approaches. ISPRS Journal of Photogrammetry and Remote Sensing, 62(6), 415-433. https://doi.org/10.1016/j.isprsjprs.2007.05.008.

Idrees, M. O., Pradhan, B. 2016a. A decade of modern cave surveying with terrestrial laser scanning: A review of sensors, method and application development. International Journal of Speleology, 45(1), 8. https://doi.org/10.5038/1827-806X.45.1.1923.

Idrees, M. O., Pradhan, B. 2016b. Hybrid Taguchi-objective function optimization approach for automatic cave bird detection from terrestrial laser scanning intensity image. International Journal of Speleology, 45(3), 9. https://doi.org/10.5038/1827-806X.45.3.1988

778 Idrees, M. O., Pradhan, B., 2017. Characterization of macro-and micro-geomorphology of cave channel from high-resolution
779 3D laser scanning survey: case study of Gomantong cave in Sabah, Malaysia, in: Karabulut, S., Çinku, M. (Eds.), Cave
780 Investigation. IntechOpen. pp 3-24. https://doi.org/10.5772/intechopen.69084.

781 Idrees, M. O., Pradhan, B., 2018. Geostructural stability assessment of cave using rock surface discontinuity extracted from
782 terrestrial laser scanning point cloud. Journal of Rock Mechanics and Geotechnical Engineering, 10(3), 534-544.
783 https://doi.org/10.1016/j.jrmge.2017.11.011.

784 Jalandoni, A., Winans, W. R., Willis, M. D., 2021. Intensity values of terrestrial laser scans reveal hidden black rock art pigment.
785 Remote Sensing, 13(7), 1357. https://doi.org/10.3390/rs13071357.

786 James, J.M., 2013. Atmospheric processes in caves. In: Shroder, J. (Editor in Chief), Frumkin, A. (Ed.), Treatise on
787 Geomorphology. Academic Press, San Diego, CA, vol. 6, Karst Geomorphology, pp. 304–318. https://doi.org/10.1016/B978-
788 0-12-374739-6.00118-4.

789 Jammes, S., Manatschal, G., Lavier, L., Masini, E., 2009. Tectono-sedimentary evolution related to extreme crustal thinning
790 ahead of a propagating ocean: example of the western Pyrenees. Tectonics 28, 4. https://doi.org/10.1029/2008TC002406.

791 Jelalian, A. V., 1992. Laser radar systems. Artech House, Boston. https://doi.org/10.1016/0021-9169(92)90171-G.

792 Kaasalainen, S., Jaakkola, A., Kaasalainen, M., Krooks, A., Kukko, A., 2011. Analysis of incidence angle and distance effects on
793 terrestrial laser scanner intensity: Search for correction methods. Remote Sensing, 3(10), 2207-2221.
794 https://doi.org/10.3390/rs3102207.

795 Kaasalainen, S., Malkamäki, T., 2020. Potential of active multispectral lidar for detecting low reflectance targets. Optics
796 Express, 28(2), 1408-1416. https://doi.org/10.1364/OE.379491.

797 Kashani, A. G., Olsen, M. J., Parrish, C. E., Wilson, N., 2015. A review of LiDAR radiometric processing: From ad hoc intensity
798 correction to rigorous radiometric calibration. Sensors, 15(11), 28099-28128. https://doi.org/10.3390/s151128099.

799 Kim, I. I., McArthur, B., Korevaar, E. J., 2001. Comparison of laser beam propagation at 785 nm and 1550 nm in fog and haze
800 for optical wireless communications. Proceedings of SPIE, Optical Wireless Communications, 4214, 26-37.
801 https://doi.org/10.1117/12.417512.

802 Kruger, A., Randolph-Quinney, P., Elliott, M., 2016. Multimodal spatial mapping and visualisation of Dinaledi Chamber and
803 Rising Star Cave. South African journal of science, 112(5-6), 1-11. https://doi.org/10.17159/sajs.2016/20160032.

Lagabrielle, Y., Bodinier, J.-L., 2008. Submarine reworking of exhumed sub-continental mantle rocks: field evidence from the Lherz peridotites, French Pyrenees: cretaceous exhumation of pyrenean mantle. Terra. Nova 20 (1), 11–21. https://doi.org/10.1111/j.1365-3121.2007.00781.x.

Lagabrielle Y., Labaume P. de Saint Blanquat M., 2010. Mantle exhumation, crustal denudation, and gravity tectonics during Cretaceous rifting in the Pyrenean realm (SW Europe): Insights from the geological setting of the lherzolite bodies. Tectonics, 29, TC4012. https://doi.org/10.1029/2009TC002588.

Lagabrielle, Y., Clerc, C., Vauchez, A., Lahfid, A., Labaume, P., Azambre, B., Fourcade, S., Dautria, J.-M., 2016. Very high geothermal gradient during mantle exhumation recorded in mylonitic marbles and carbonate breccias from a Mesozoic Pyrenean palaeomargin (Lherz area, North Pyrenean Zone, France). Comptes Rendus Geosciences, 348, 257–267. https://doi.org/10.1016/j.crte.2015.11.004.

Lagabrielle, Y., Asti, R., Fourcade, S., Corre, B., Poujol, M., Uzel, J., Labaume, P., Clerc, C., Lafay, R., Picazo, S., Maury, R., 2019a. Mantle exhumation at magma-poor passive continental margins. Part I. 3D architecture and metasomatic evolution of a fossil exhumed mantle domain (Urdach lherzolite, North-Western Pyrenees, France). BSGF - Earth Sci. Bull. 190, 8. https://doi.org/10.1051/bsgf/2019007.

Lagabrielle, Y., Asti, R., Fourcade, S., Corre, B., Uzel, J., Labaume, P., Clerc, C., Lafay, R., Picazo, S., 2019b. The mechanisms of mantle exhumation at magma-poor passive continental margins. Part II. Insights from high-displacement, low-angle faults preserved in a fossil distal margin domain (Saraillé lherzolites, north-western Pyrenees, France). BSGF Earth Sci. Bull. 190, 14. https://doi.org/10.1051/bsgf/2019013.

Landeschi, G., Apel, J., Lundström, V., Storå, J., Lindgren, S., Dell'Unto, N., 2019. Re-enacting the sequence: combined digital methods to study a prehistoric cave. Archaeological and anthropological sciences, 11(6), https://doi.org/10.1007/s12520-018-0724-5.

Laukamp, C., Termin, K. A., Pejcic, B., Haest, M., Cudahy, T., 2012. Vibrational spectroscopy of calcic amphiboles–applications for exploration and mining. European Journal of Mineralogy, 24(5), 863-878. https://doi.org/10.1127/0935-1221/2012/0024-2218.

Le Roux, V., Bodinier, J. L., Tommasi, A., Alard, O., Dautria, J. M., Vauchez, A., Riches, A. J. V., 2007. The Lherz spinel lherzolite: refertilized rather than pristine mantle. Earth and Planetary Science Letters, 259(3-4), 599-612. https://doi.org/10.1016/j.epsl.2007.05.026.

Liu, D., Yu, J., 2009. Otsu method and K-means. In 2009 Ninth International Conference on Hybrid Intelligent Systems (Vol. 1, pp. 344-349). IEEE. https://doi.org/10.1109/HIS.2009.74.

Lorenz, S., Ghamisi, P., Kirsch, M., Jackisch, R., Rasti, B., Gloaguen, R., 2021. Feature extraction for hyperspectral mineral domain mapping: A test of conventional and innovative methods. Remote Sensing of Environment, 252, 112129. https://doi.org/10.1016/j.rse.2020.112129.

Masini, E., Manatschal, G., Tugend, J., Mohn, G., Flament, J.-M., 2014. The tectonosedimentary evolution of a hyper-extended rift basin: the example of the Arzacq–Mauléon rift system (Western Pyrenees, SW France). Int. J. Earth Sci. 103 (6), 1569–1596. https://doi.org/10.1007/s00531-014-1023-8.

Matasci, B., Carrea, D., Abellan, A., Derron, M. H., Humair, F., Jaboyedoff, M., Metzger, R., 2015. Geological mapping and fold modeling using Terrestrial Laser Scanning point clouds: application to the Dents-du-Midi limestone massif (Switzerland). European Journal of Remote Sensing, 48(1), 569-591. https://doi.org/10.5721/EuJRS20154832.

McFarlane, D. A., Roberts, W., Buchroithner, M., Van Rentergem, G., Lundberg, J., Hautz, S., 2015. Terrestrial LiDAR-based automated counting of swiftlet nests in the caves of Gomantong, Sabah, Borneo. International Journal of Speleology, 44(2), 6. https://doi.org/10.5038/1827-806X.44.2.8.

Milius, J., Petters, C., 2012. Eisriesenwelt–From laser scanning to photo-realistic 3D model of the biggest ice cave on Earth. In GI-Forum (pp. 513-523).

Monchoux, P., 1970. Les lherzolites Pyrénéennes: Contribution à l'étude de leur minéralogie, de leur genèse et de leurs transformations, Ph.D. thesis, Univ. of Toulouse, Toulouse, France.

Nayar, S.K., Ikeuchi, K., Kanade, T., 1991. Surface reflection: physical and geometrical perspectives. IEEE Transactions on Pattern Analysis and Machine Intelligence, vol. 13, no. 7, pp. 611-634. https://doi.org/10.1109/34.85654.

Nolan, R., Alvarez, L., Padilla-Parra, S., Landini, G., 2022. autothresholdr: an R port of the ImageJ plugin "Auto Threshold".

Núñez, M. A., Buill, F., Edo, M., 2013. 3D model of the Can Sadurní cave. Journal of archaeological Science, 40(12), 4420-4428. https://doi.org/10.1016/j.jas.2013.07.006.

Oren, M., Nayar, S.K., 1994. Seeing beyond Lambert's law. In: Eklundh, J.-O. (Ed.), Computer vision — ECCV '94, Lecture Notes in Computer Science. Springer-Verlag, Berlin/Heidelberg, pp. 269–280. http://dx.doi.org/10.1007/BFb0028360.

Oren, M., Nayar, S. K., 1995. Generalization of the Lambertian model and implications for machine vision. International Journal of Computer Vision, 14(3), 227-251. https://doi.org/10.1007/BF01679684.

Otsu, N., 1979. A threshold selection method from gray-level histograms. IEEE Trans. Sys. Man. Cyber. 9 (1): 62-66. https://doi.org/10.1109/tsmc.1979.4310076.

Penasa, L., Franceschi, M., Preto, N., Teza, G., Polito, V., 2014. Integration of intensity textures and local geometry descriptors from Terrestrial Laser Scanning to map chert in outcrops. ISPRS Journal of Photogrammetry and Remote Sensing, 93, 88-97. https://doi.org/10.1016/j.isprsjprs.2014.04.003.

Pfennigbauer, M., Ullrich, A., 2010. Improving quality of laser scanning data acquisition through calibrated amplitude and pulse deviation measurement. Proceedings of SPIE, 7684, 76841F. https://doi.org/10.1117/12.849641.

RIEGL Laser Measurement Systems GmbH, 2015. 3D Terrestrial laser scanner RIEGL VZ-400/RIEGL VZ-1000/RIEGL VZ-2000 General Description and Data Interfaces.

RIEGL Laser Measurement Systems GmbH, 2017. LAS Extrabytes Implementation in RIEGL Software Whitepaper.

Rees, W. G., 2013. Physical principles of remote sensing (3rd ed.). Cambridge university press. https://doi.org/10.1017/CBO9781139017411

Saint Blanquat, M., Bajolet, F., Grand'Homme, A., Proietti, A., Zanti, M., Boutin, A., Clerc, C., Lagabrielle, Y., Labaume, P., 2016. Cretaceous mantle exhumation in the central Pyrenees: new constraints from the peridotites in eastern Ariège (North Pyrenean zone, France). Comptes Rendus Géoscience, 348(3-4), 268-278. https://doi.org/10.1016/j.crte.2015.12.003

Santo, A., Budetta, P., Forte, G., Marino, E., Pignalosa, A., 2017. Karst collapse susceptibility assessment: A case study on the Amalfi Coast (Southern Italy). Geomorphology, 285, 247-259. https://doi.org/10.1016/j.geomorph.2017.02.012.

Saspiturry, N., Razin, P., Baudin, T., Serrano, O., Issautier, B., Lasseur, E., Allanic, C., Thinon, I., Leleu, S., 2019. Symmetry vs. asymmetry of a hyper-thinned rift: Example of the Mauléon Basin (Western Pyrenees, France). Marine and Petroleum Geology, 104, 86–105. https://doi.org/10.1016/j.marpetgeo.2019.03.031.

Saspiturry, N., Allanic, C., Razin, P., Issautier, B., Baudin, T., Lasseur, E., Serrano, O., Leleu, S., 2020a. Closure of a hyperextended system in an orogenic lithospheric pop-up, Western Pyrenees: The role of mantle buttressing and rift structural inheritance. Terra Nova, 32(4), 253–260. https://doi.org/10.1111/ter.12457.

Saspiturry, N., Lahfid, A., Baudin, T., Guillou-Frottier, G., Razin, P., Issautier, B., Le Bayon, B., Serrano, O., Lagabrielle, Y., Corre, B., 2020b. Paleogeothermal gradients across an inverted hyperextended rift system: Example of the mauléon fossil rift (Western Pyrenees). Tectonics, 39(10), 1–36. https://doi.org/10.1029/2020TC006206.

Silvestre, I., Rodrigues, J. I., Figueiredo, M., Veiga-Pires, C., 2015. High-resolution digital 3D models of Algar do Penico Chamber: limitations, challenges, and potential. International Journal of Speleology, 44(1), 25-35. https://doi.org/10.5038/1827-806X.44.1.3.

Soudarissanane, S., Lindenbergh, R., Menenti, M., Teunissen, P., 2011. Scanning geometry: Influencing factor on the quality of terrestrial laser scanning points. ISPRS Journal of Photogrammetry and Remote Sensing, 66(4), 389-399. https://doi.org/10.1016/j.isprsjprs.2011.01.005.

Sorriaux, P., Guinot, R., Ferré, E., Gallay, M., Šupinský, J., de Saint Blanquat, M., Asti, R., 2019. Expédition spéléo-scientifique au gouffre Georges: Relevé 3D de la Grande galerie. Spelunca, 5, 5-13.

Šupinský, J., Kaňuk, J., Hochmuth, Z., Gallay, M., 2019. Detecting dynamics of cave floor ice with selective cloud-to-cloud approach. The Cryosphere, 13(11), 2835-2851. https://doi.org/10.5194/tc-13-2835-2019.

Šupinský, J., Kaňuk, J., Nováková, M., Hochmuth, Z., 2022. LiDAR point clouds processing for large-scale cave mapping: a case study of the Majko dome in the Domica cave. Journal of Maps, 1-8. https://doi.org/10.1080/17445647.2022.2035270.

Tan, K., Cheng, X., Ding, X., Zhang, Q., 2015. Intensity data correction for the distance effect in terrestrial laser scanners. IEEE Journal of Selected Topics in Applied Earth Observations and Remote Sensing, 9(1), 304-312. https://doi.org/10.1109/JSTARS.2015.2497310.

Tan, K., Cheng, X., 2016. Correction of incidence angle and distance effects on TLS intensity data based on reference targets. Remote Sensing, 8(3), 251. https://doi.org/10.3390/rs8030251.

Tan, K., Cheng, X., Cheng, X., 2016. Modeling hemispherical reflectance for natural surfaces based on terrestrial laser scanning backscattered intensity data. Optics express, 24(20), 22971-22988. https://doi.org/10.3390/rs9080853.

Tavani S, Bertok C, Granado P, Piana F, Salas R, Vigna B, Muñoz JA., 2018. The Iberia-Eurasia plate boundary east of the Pyrenees. Earth-Science Reviews 187, 314–337. https://doi.org/10.1016/j.earscirev.2018.10.008.

Teo, T. A., Yu, H. L., 2015. Empirical radiometric normalization of road points from terrestrial mobile LiDAR system. Remote Sensing, 7(5), 6336-6357. https://doi.org/10.3390/rs70506336.

Thiele, S. T., Lorenz, S., Kirsch, M., Acosta, I. C. C., Tusa, L., Herrmann, E., Möckel, R., Gloaguen, R. 2021. Multi-scale, multi-sensor data integration for automated 3-D geological mapping. Ore Geology Reviews, 104252. https://doi.org/10.1016/j.oregeorev.2021.104252.

Triantafyllou, A., Watlet, A., Le Mouélic, S., Camelbeeck, T., Civet, F., Kaufmann, O., Quinif, Y., Vandycke, S., 2019. 3-D digital outcrop model for analysis of brittle deformation and lithological mapping (Lorette cave, Belgium). Journal of Structural Geology, 120, 55-66. https://doi.org/10.1016/j.jsg.2019.01.001.

Ullrich, A.; Schwarz, R.; Kager, H., 2003. Using hybrid multi-station adjustment for an integrated camera laser-scanner system. Opt. 3-D Meas. Tech. IV, 1, 298–305.

Vergés, J., Fernàndez, M., Martìnez, A., 2002. The Pyrenean orogen: pre-, syn-, and post-collisional evolution. Journal of the Virtual Explorer, 8, 55-74. https://doi.org/10.3809/JVIRTEX.2002.00058.

Wagner, W., Ullrich, A., Ducic, V., Melzer, T., Studnicka, N., 2006. Gaussian decomposition and calibration of a novel small-footprint full-waveform digitising airborne laser scanner. ISPRS Journal of Photogrammetry and Remote Sensing, 60(2), 100-112. https://doi.org/10.1016/j.isprsjprs.2005.12.001.

Wagner, W., 2010. Radiometric calibration of small-footprint full-waveform airborne laser scanner measurements: Basic physical concepts. ISPRS Journal of Photogrammetry and Remote Sensing, 65(6), 505-513. https://doi.org/10.1016/j.isprsjprs.2010.06.007.

Xu, T., Xu, L., Yang, B., Li, X., Yao, J., 2017. Terrestrial laser scanning intensity correction by piecewise fitting and overlap-driven adjustment. Remote Sensing, 9(11), 1090. https://doi.org/10.3390/rs9111090.

Živec, T., Anžur, A., Verbovšek, T., 2019. Determination of rock type and moisture content in flysch using TLS intensity in the Elerji quarry (south-west Slovenia). Bulletin of Engineering Geology and the Environment, 78(3), 1631-1643. https://doi.org/10.1007/s10064-018-1245-2.

List of Figure Captions

Fig. 1. Location of the Gouffre Georges. Selected parts for the TLS survey (red) of the Gouffre Georges cave complex (orange) are accessible via the entrance Tube at the altitude of 1390 m. The photographs A, B, C illustrate the cave space and surveying conditions in different parts located in the map. Base map: ©2021 Esri

Fig. 2. Schematic workflow of processing the data obtained by TLS survey and experimental scanning and subsequent parameter estimation for the intensity correction.

Fig. 3. The top view and side view of the laser-scanned part of Gouffre Georges comprising the domes of Salle de la Famine and Grande Galerie accessible via the Tube entrance with marked TLS positions (red dots) and cave exterior (green).

Fig. 4. Scene of the calibration experiment showing the position of the scanner with respect to the scanned white target for distances from 2.5 to 60 m. Recorded intensity decreases for longer ranges.

Fig. 5. Mean values of the recorded laser intensity of the reference target as the function of scanning range acquired by the RIEGL VZ-1000 in the laboratory experiment. The vertical bars show standard deviations of intensity measurements.

Fig. 6. Differences between intensity values of various incidence angles corrected using different σ_{slope} values for lherzolite and marble samples.

Fig. 7. Distribution of laser intensity data recorded from three overlapping scanning positions, i.e., three different ranges (41.1 m, 32.9 m, 21.5 m) capturing the same cave wall in the Salle de la Famine dome: (A) raw intensities, (B) intensities after the correction for distance and incidence angle, (C) final intensity values after the correction for the atmospheric attenuation.

Fig. 8. Final point cloud comprising of 47 scanning positions coloured by the (A) range values (B) original intensity (C) corrected intensity.

Fig. 9. Top and side view of the selected Gouffre Georges cave parts point cloud with corrected intensity values after removing the outliers by the denoising, revealing the lithological contacts and the strong water occurrence. The dashed line in the scatterplot indicates the boundary between marble and lherzolite.

Fig. 10. Results of scanning of the (A) lherzolite and (B) marble samples: distribution of the original intensities for the samples of (C) lherzolite and (D) marble, and the distribution of the corrected intensities for the samples of (E) lherzolite and (F) marble, each observed under the dry and wet surface conditions. The blue bell-shaped curve indicates normal distribution model based on the sample mean and standard deviation as reported in Tab. 7 and vertical dashed and solid lines, respectively.

Fig. 11. Section of the 3D TLS point cloud from Grande Galerie (Fig. 9) comprising a cave wall coloured by (A) photographed natural colours with dark lherzolite and light marble, (B) the corrected intensity values, (C) classification based on the thresholds from corrected intensities of the rock samples, (D) classification based on the thresholds from the histogram of the corrected intensity of the cave, (E) classification based on the Otsu thresholding, and (F) classification based on the K-means clustering.

Fig. 12. Results of the material differentiation based on the histogram clustering applied individually on the segmented cave sections.